J. Fluid Mech. (2014), *vol.* 751, *pp.* 432–479.
doi:10.1017/jfm.2014.312

Perturbation theory and numerical modelling of weakly and moderately nonlinear dynamics of the incompressible Richtmyer–Meshkov instability

A. L. Velikovich[1],†, M. Herrmann[2] and S. I. Abarzhi[3],‡

[1]Plasma Physics Division, Naval Research Laboratory, Washington, DC 20375, USA

[2]Arizona State University, Tempe, AZ 85287, USA

[3]Carnegie Mellon University, Pittsburgh, PA 15213, USA, and
Carnegie Mellon University Qatar, Education City, Doha, Qatar

(Received 18 July 2013; revised 18 March 2014; accepted 29 May 2014;
first published online 23 June 2014)

A study of incompressible two-dimensional (2D) Richtmyer–Meshkov instability (RMI) by means of high-order perturbation theory and numerical simulations is reported. Nonlinear corrections to Richtmyer's impulsive formula for the RMI bubble and spike growth rates have been calculated for arbitrary Atwood number and an explicit formula has been obtained for it in the Boussinesq limit. Conditions for early-time acceleration and deceleration of the bubble and the spike have been elucidated. Theoretical time histories of the interface curvature at the bubble and spike tip and the profiles of vertical and horizontal velocities have been calculated and favourably compared to simulation results. In our simulations we have solved 2D unsteady Navier–Stokes equations for immiscible incompressible fluids using the finite volume fractional step flow solver NGA developed by Desjardins *et al.* (*J. Comput. Phys.*, vol. 227, 2008, pp. 7125–7159) coupled to the level set based interface solver LIT (Herrmann, *J. Comput. Phys.*, vol. 227, 2008, pp. 2674–2706). We study the impact of small amounts of viscosity on the flow dynamics and compare simulation results to theory to discuss the influence of the theory's ideal inviscid flow assumption.

Key words: fingering instability, nonlinear instability, shock waves

1. Introduction

The Richtmyer–Meshkov instability (RMI) develops when a shock wave interacts with an interface between two fluids with different values of the acoustic impedance (Richtmyer 1960; Meshkov 1969), or, in the incompressible case, when a fluid interface undergoes impulsive acceleration (Jacobs & Sheeley 1996; Velikovich & Dimonte 1996; Niederhaus & Jacobs 2003; Zabusky *et al.* 2003; Likhachev & Jacobs 2005; Mueschke *et al.* 2005; Chapman & Jacobs 2006; Cotrell & Cook 2007; Abarzhi 2008; Olson & Jacobs 2009). Extensive interfacial mixing of the fluids ensues with

† Email address for correspondence: sasha.velikovich@nrl.navy.mil

‡ The original version of this article was published with the incorrect affiliation for S. I. Abarzhi. A notice detailing this has been published online and in print, and the error rectified in the online PDF and HTML copies.

time. The interfacial mixing plays an important role in a variety of phenomena in nature and technology including the formation of a hot spot in inertial confinement fusion, supernova core collapse and material transformation under impact (Bodner *et al.* 1998; Brouillette 2002; Meshkov 2006; Remington, Drake & Ryutov 2006; Drake 2009; Abarzhi 2010; Aglitskiy *et al.* 2010; Nishihara *et al.* 2010). Interfacial mixing strongly influences the transport of mass, momentum and energy in the fluid flow and the interplay of its scalar and vector fields, see Kadau *et al.* (2010), Stanic *et al.* (2012), Abarzhi, Gauthier & Sreenivasan (2013), Anisimov *et al.* (2013), Meshkov (2013) and Stanic *et al.* (2013).

For RMI in compressible fluids, refraction of an incident shock wave at the perturbed fluid interface results in deposition of vorticity at the shocked interface. This localized vorticity is the main driver of the interfacial Richtmyer–Meshkov (RM) perturbation growth. In the incompressible case, a similar growth is triggered by the instantaneous velocity perturbation imposed on the fluids (or a single fluid with a rippled surface) by an 'impulsive acceleration'. The latter case has much in common with the classical Rayleigh–Taylor instability (RTI) for a particular case of a short acceleration pulse $g = U\delta(t)$, where U is the velocity instantly acquired by the interface and the fluid(s) bounded by it, and $\delta(t)$ is the delta function. It can also be regarded as a limiting case of compressible RMI driven by a very weak incident shock wave refracting at a slightly perturbed interface.

Having started with the seminal work of Richtmyer (1960), extensive theoretical studies significantly advanced our understanding of RMI dynamics. For the linear, small-amplitude regime of compressible RMI, comprehensive theory makes it possible to calculate exactly (i.e. with any desired precision) all relevant perturbation amplitudes. These include the interfacial ripple amplitude, the ripple velocity, the late-time asymptotic value of the latter (that is, the linear RM growth rate), the perturbation evolution in the outgoing shock and/or rarefaction waves and the time-dependent perturbed fields of all the fluid variables between the interface and the outgoing wavefronts; see Kivity & Hanin (1981), Fraley (1986), Grove *et al.* (1993), Yang, Zhang & Sharp (1994), Velikovich (1996), Velikovich & Phillips (1996), Wouchuk (2001*a*,*b*), Wouchuk & Carretero (2004), Griffond (2006), Nishihara *et al.* (2010) and references therein.

A theory of nonlinear RMI has only been developed for the incompressible case. This is due to the huge complexity of specifically compressible nonlinear phenomena, such as secondary shock waves, see Holmes *et al.* (1999). Fortunately, the incompressible approximation works reasonably well for RMI (see Zhang & Sohn (1997*a*), Kotelnikov, Ray & Zabusky (2000), Carlès & Popinet (2001), Zabusky *et al.* (2003), Herrmann, Moin & Abarzhi (2008), Abarzhi (2008), Dimonte & Ramaprabhu (2010), Stanic *et al.* (2012) and references therein). Indeed, after some relatively short transient period, the acoustic interaction of the interface with the outgoing waves becomes small, and interfacial growth is dominated by the divergence-free perturbation modes (Wouchuk 2001*a*,*b*) and is relatively well captured by the incompressible potential-flow model. This model is directly applicable to experiments with liquids or jellies (Niederhaus & Jacobs 2003; Meshkov 2006), particularly when the RMI is triggered by a prescribed acceleration history (linear electric motor in Dimonte *et al.* (1996), Dimonte (1999); magnetorheological fluids in White *et al.* (2010)) and to the RMI developing at the rippled rear surface of a condensed material, which melts after the passage of a strong shock wave; see (Bakhrakh *et al.* 2006; Aprelkov *et al.* 2010; Dimonte *et al.* 2011; Aglitskiy *et al.* 2012; Buttler *et al.* 2012).

The incompressible perturbation equations are not exactly integrable. Various approaches have been developed to construct their approximate solutions. Since

potential flow permits fluid equations to be formulated in terms of boundary motion, nonlinear RMI evolution is described by a solution of a non-stationary one-dimensional problem, which can be addressed using the mathematical formalism of conformal mapping (Menikoff & Zemach 1983), vortex methods (Neuvazhaev & Parshukov 1992), Birkhoff–Rott (Matsuoka & Nishihara 2006) or other integro-differential equations (Volkov, Maĭer & Yalovets 2001, 2003), or Lagrangian Fourier expansions (Hazak 1996). In any of these cases, a numerical scheme must be developed to obtain a solution. An alternative approach is to construct a solution of the nonlinear equations as a formal perturbation series. This approach to the dynamics of fluid interfaces was pioneered by Stokes (1849) and followed by many researchers who studied gravity waves; see Schwartz (1974), Cokelet (1977), Holyer (1979), and references therein. Later it was applied to the physics of interfacial instabilities (Rosenhead 1931; Ingraham 1954; Emmons, Chang & Watson 1960; Jacobs & Catton 1988; Zufiria 1988; Haan 1991; Mikaelian 1994; Hazak 1996; Velikovich & Dimonte 1996; Zhang & Sohn 1996, 1997*a*,*b*; Berning & Rubenchik 1998; Holmes *et al.* 1999; Vandenboomgaerde, Gauthier & Mügler 2002; Zabusky *et al.* 2003; Matsuoka 2010). One can obtain exact expressions for the first several nonlinear terms with essentially algebraic manipulations, both for RMI and RTI, the procedure and the results being much simpler in the former case.

As is often the case with perturbation analysis applied to a nonlinear problem, the challenge is to obtain a sufficiently accurate approximate solution of the problem with a finite, exact but inevitably incomplete set of perturbation terms. There is no consensus in the literature on the validity and physical significance of perturbation theory applied to RMI and RTI. On the one hand, early in its development, some authors expressed an over-pessimistic view that the perturbation series might be always divergent and thereby have little physical meaning (Ingraham 1954). On the other hand, the popular Layzer model proposed at approximately the same time (Layzer 1955) is based on the over-optimistic assumption that the first order terms of the series encode enough information to describe the instability development from the early, weakly nonlinear stage up to late times. Explicit formulas based on Layzer (1955) or Zufiria's (1988) models for RMI and RTI have been reported in many publications (Hecht, Alon & Shvarts 1994; Mikaelian 1998; Zhang 1998; Goncharov 2002; Mikaelian 2003; Sohn 2004; Mikaelian 2008; Sohn 2009). These formulas were also applied in other phenomenological heuristic expressions, including those obtained from drag buoyancy-models (Alon *et al.* 1995; Sadot *et al.* 1998; Oron *et al.* 2001). Such formulas in many cases provide a reasonable description of weakly-to-moderately nonlinear RMI and RTI. However, they are obviously not suitable for code verification because their accuracy cannot be evaluated *a priori*.

As noted by Zhang & Sohn (1999), 'At this order [4th], the expansion is rather complicated and inclusion of higher order terms is avoided'. To obtain meaningful results with perturbation theory, one has to overcome this difficulty by calculating a large number of high-order terms, which is possible. The researchers who studied gravity waves extended the Stokes perturbation expansion (Stokes 1849) to orders over 100 (Schwartz 1974; Cokelet 1977). Such calculations are significantly simplified by means of symbolic computation. High-order perturbation series in the RMI problem have been demonstrated to converge for small values of the perturbation parameters, thereby generating analytic functions. In most cases such functions can be analytically continued beyond their circles of convergence, which is conveniently done with the aid of Padé approximation, e.g. see Bender & Orszag (1978) and Baker & Grave-Morris (1981). This approach has also been pioneered in the theory of gravity

waves (Schwartz 1974). In the nonlinear theory of RMI high-order perturbation series analysis was first used by Velikovich & Dimonte (1996), Holmes *et al.* (1999), and then by Vandenboomgaerde *et al.* (2002) and Zabusky *et al.* (2003). The highest perturbation orders used in this problem so far were 20 for $A = 1$ (Velikovich & Dimonte 1996), 10 for general theory with arbitrary A (Zabusky *et al.* 2003) and 11 for simplified theory with arbitrary A (Vandenboomgaerde *et al.* 2002). Our expansions used in this article are based on general perturbation theory for arbitrary A developed to order 22.

The resulting set of perturbation terms is extensive enough to test the convergence of successive diagonal Padé approximants. This makes it possible to provide theoretical estimates accurate to within 1 % for both bubbles and spikes up to finite dimensional amplitudes $k\eta \sim 1$–2, which is in the moderately nonlinear regime. The range of convergence of analytically continued perturbation functions is always limited, sometimes by the highest perturbation order available for approximation, but emergence of a singularity is also possible, cf. Pelz & Gulak (1997). There is no way to draw a definitive conclusion on the late-time behaviour of RMI based on three or any other finite number of perturbation terms. To describe the late-time asymptotics, a different theoretical approach is needed (Abarzhi 2002; Abarzhi, Nishihara & Glimm 2003; Abarzhi 2008).

In this work we study weakly and moderately nonlinear two-dimensional (2D) incompressible RMI evolution by comparing numerical simulations with analysis based on perturbation theory. To eliminate the uncertainty involved in approximating RMI development after shock-interface interaction in a compressible fluid by the incompressible theoretical model, in our simulations we solve the Navier–Stokes equation for 2D two-phase incompressible flow and employ a refined level set method to model the motion of the immiscible interface. Regularization of the ideal-fluid simulation with viscosity is necessary to avoid generation of flow structures in the simulation that are numerical artifacts. Appropriately decreasing viscosity in the simulations to approach the ideal inviscid conditions of the theory, we demonstrate good convergence of numerical results to the theoretical predictions. Including viscosity in the numerical simulations, we furthermore study its effect on RMI evolution, to answer the question of how limiting the assumption of inviscid flow is to the application of the theory to cases with realistic, non-zero viscosity fluids.

We find a number of new features of a weakly and moderately nonlinear RMI that are not captured by simplified and *ad hoc* phenomenological models. These include the effect of the initial amplitude and the density ratio on the bubble and spike dynamics, such as the presence or absence of early-time acceleration of the spike and the bubble, and the quantitative velocity flow field. Our results suggest that reliable numerical modelling of RMI development requires careful control of the regularization, grid refinement, and capturing of the interface.

This paper is organized as follows. In § 2 we summarize the results of the theory. Section 3 describes the numerical method and the computational set-up. Section 4 presents the simulation results compared to theoretical predictions. In § 5 we conclude with a discussion.

2. Theory

2.1. *Governing equations*

Below we briefly describe the nonlinear high-order perturbation theory of the 2D RMI as first derived by Velikovich & Dimonte (1996) for Atwood number $A = 1$. Some

results of its generalization for arbitrary A have already been published by Holmes *et al.* (1999).

Incompressible 2D RMI or RTI flows (Rosenhead 1931; Ingraham 1954) are described by Bernoulli's equation

$$(\rho_2-\rho_1)\eta g(t)-\rho_1\left[\frac{\partial\Phi_1}{\partial t}+\frac{1}{2}(\nabla\Phi_1)^2\right]+\rho_2\left[\frac{\partial\Phi_2}{\partial t}+\frac{1}{2}(\nabla\Phi_2)^2\right]=0 \tag{2.1}$$

and by the kinematic conditions

$$\frac{\partial\eta}{\partial t}=\frac{\partial\Phi_1}{\partial y}-\frac{\partial\eta}{\partial x}\frac{\partial\Phi_1}{\partial x}=\frac{\partial\Phi_2}{\partial y}-\frac{\partial\eta}{\partial x}\frac{\partial\Phi_2}{\partial x}, \tag{2.2}$$

which should be satisfied at the perturbed interface $y=\eta(x,t)$. Here ρ_1, Φ_1 and ρ_2, Φ_2 are densities and velocity potentials of the lower $[y<\eta(x,t)]$ and upper $[y>\eta(x,t)]$ fluid layers, respectively; $g(t)$ is the gravity acceleration in the negative y direction. The Atwood number is defined as $A=(\rho_2-\rho_1)/(\rho_2+\rho_1)$. We are interested in the perturbations localized near the interface, so that the velocity potentials $\Phi_{1,2}(x,y,t)$ vanish in the limits $y\to\mp\infty$, respectively.

The RMI case is specified by the choice of impulsive gravity acceleration:

$$g(t)=U\delta(t). \tag{2.3}$$

Initially, both fluids are at rest. We specify a single-mode 2D initial perturbation by

$$\eta(x,t<0)=\eta_0\cos(kx). \tag{2.4}$$

We choose the units of length and time as k^{-1} and $(kAU)^{-1}$, respectively (note that such choice of the time unit implies that the normalized time grows in the negative direction if $A<0$). We normalize the interface displacement by η_0, introducing dimensionless displacement amplitude

$$\xi(x,t)=\frac{\eta(x,t)}{\eta_0}, \tag{2.5}$$

and the velocity potentials by η_0AU:

$$\phi_{1,2}(x,y,t)=\frac{\Phi_{1,2}(x,y,t)}{\eta_0AU}. \tag{2.6}$$

The perturbation parameter is defined as

$$\varepsilon=k\eta_0. \tag{2.7}$$

Then Bernoulli's equation (2.1) is transformed to

$$2\xi\delta(t)+(A-1)\left[\frac{\partial\phi_1}{\partial t}+\frac{\varepsilon}{2}(\nabla\phi_1)^2\right]+(A+1)\left[\frac{\partial\phi_2}{\partial t}+\frac{\varepsilon}{2}(\nabla\phi_2)^2\right]=0. \tag{2.8}$$

One of the kinematic conditions (2.2) is used directly as

$$\frac{\partial\xi}{\partial t}=\frac{\partial\phi_2}{\partial y}-\varepsilon\frac{\partial\xi}{\partial x}\frac{\partial\phi_2}{\partial x}, \tag{2.9}$$

whereas the other is accounted for in the form of the following compatibility condition:

$$\frac{\partial \phi_1}{\partial y} - \frac{\partial \phi_2}{\partial y} = \varepsilon \left(\frac{\partial \phi_1}{\partial x} - \frac{\partial \phi_2}{\partial x} \right) \frac{\partial \xi}{\partial x}. \tag{2.10}$$

Equations (2.8)–(2.10) should be satisfied at the interface $y = \varepsilon\xi(x, t)$. The dimensionless velocity potentials $\phi_{1,2}(x, y, t)$ are harmonic functions which satisfy the boundary conditions

$$\phi_{1,2}(x, y, t) \to 0 \quad \text{at } y \to \mp\infty. \tag{2.11}$$

At $t < 0$ both fluids are at rest, hence the velocity potentials are coordinate-independent, or, equivalently, identically zero. At $t > 0$, the acceleration term in (2.8) is zero. To relate the magnitude of the impulsive acceleration to subsequent fluid motion, we integrate (2.8) from $t = 0^-$ to $t = 0^+$ (subsequently, $t = 0$ always means $t = 0^+$) and obtain the initial conditions:

$$\xi(x, 0) = \cos(x), \tag{2.12}$$

$$2\cos(x) + (A - 1)\phi_1(x, \varepsilon\cos(x), 0) + (A + 1)\phi_2(x, \varepsilon\cos(x), 0) = 0. \tag{2.13}$$

The above equations describing a potential flow of two ideal incompressible fluids separated by an immiscible interface constitute the basis of all theoretical approaches used to analyse experimental data and numerical simulation results for RMI. Their accurate numerical solution can be obtained by a number of formally different mathematical techniques which, if applied correctly, should generate physically equivalent results (Menikoff & Zemach 1983; Neuvazhaev & Parshukov 1992; Hazak 1996; Volkov *et al.* 2001, 2003; Matsuoka & Nishihara 2006). Analytical approximations to their solutions are sought with the aid of Layzer (Mikaelian 1998; Zhang 1998; Goncharov 2002; Mikaelian 2003; Sohn 2003; Mikaelian 2008), Zufiria (Sohn 2004, 2008), the steady-state vortex (Jacobs *et al.* 1995; Jacobs & Sheeley 1996; Likhachev & Jacobs 2005) and drag-buoyancy (Alon *et al.* 1994; Hecht *et al.* 1994; Alon *et al.* 1995; Sadot *et al.* 1998; Oron *et al.* 2001) models. Some authors use initial conditions different from (2.12) and (2.13) (which are appropriate for a delta-shaped acceleration pulse (2.3)), seeking to better approximate the aftermath of the shock refraction at a rippled material interface (Zhang & Sohn 1996, 1997*a*,*b*, 1999; Rikanati *et al.* 2003; Zabusky *et al.* 2003). Their results are thereby different from ours. In the present work we emphasize the (almost) exact solution of the problem formulated above. All the perturbation terms are calculated exactly. As demonstrated below, the results of this theory could be meaningfully compared to experimental data, numerical results or predictions of other nonlinear theories, either when the perturbation series converge, or when the functions generated by the diverging series can be analytically continued with sufficient accuracy.

2.2. *Perturbation expansion*

We seek a solution of (2.8)–(2.10) with the boundary conditions (2.11) and the initial conditions (2.12), (2.13) expressed as formal power series in ε:

$$\xi(x, t) = \sum_{m=0}^{\infty} \varepsilon^m \xi_m(x, t); \quad \phi_{1,2}(x, y, t) = \sum_{m=0}^{\infty} \varepsilon^m \phi_{1,2}^{(m)}(x, y, t). \tag{2.14a,b}$$

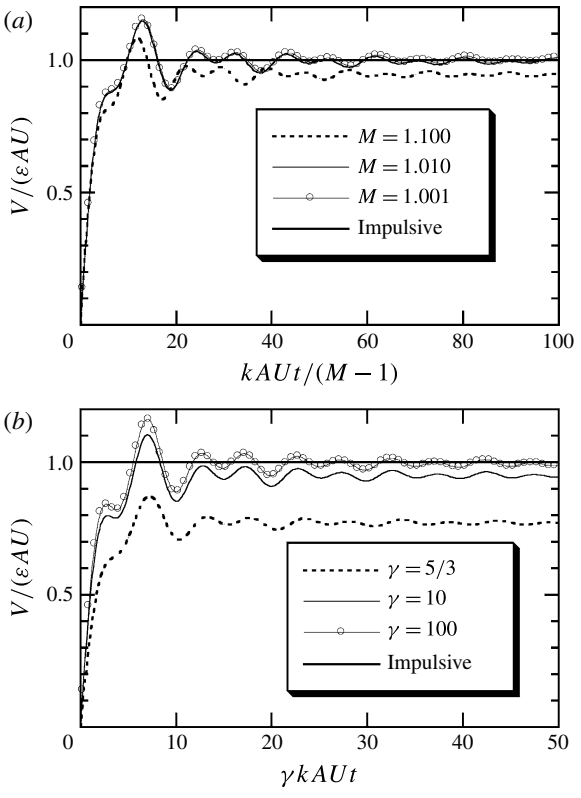

FIGURE 1. Transition from the evolution of the small-amplitude compressible RM growth rate to the limit of impulsive acceleration. Normalized growth rate vs. normalized time calculated for Atwood number $A = 0.55$: (*a*) $\gamma_1 = \gamma_2 = 5/3$, varied Mach number M of the incident shock wave; (*b*) Mach number $M = 1.5$, varied $\gamma_1 = \gamma_2 = \gamma$. The horizontal line $V/(\varepsilon AU) = 1$ corresponds to the Richtmyer impulsive model.

We address the issues of convergence and analytic continuation of formal expansions (2.14) after the coefficients of the expansion are calculated; see below. The solution proceeds as described in Ingraham (1954) and Velikovich & Dimonte (1996). It represents a straightforward generalization of the solution presented by Velikovich & Dimonte (1996) for arbitrary Atwood number A.

The results of the calculation for the displacement amplitude are, to first order:

$$\xi_0(x, t) = (t + 1)\cos(x). \tag{2.15}$$

This result reproduces the well-known linear Richtmyer formula for impulsive acceleration (Richtmyer 1960), as it should. Indeed, since in the linear approximation the incompressible regime can be regarded as the weak-shock limit of the more general compressible case, in this limit, as demonstrated by Fraley (1986) and Wouchuk (2001*a*,*b*), Richtmyer's formula is accurate and coincides with all other prescriptions (Meyer & Blewett 1972; Vandenboomgaerde, Mügler & Gauthier 1998). Figure 1 illustrates this limiting transition from the fully compressible small-amplitude theory of RMI perturbation evolution to the incompressible growth described by

Richtmyer's formula for weak shock waves (a) and weak shock compressibility (b). Here we plot the time-dependent linear RMI growth rate V (Velikovich 1996) normalized with respect to εAU, which is the dimensional Richtmyer's formula prediction, vs. appropriately normalized time. In figure 1(a) we show how the growth rate evolution changes as the incident shock Mach number M is reduced from 1.1 to 1.01, to 1.001, while the Atwood number $A = 0.55$ and $\gamma_1 = \gamma_2 = 5/3$ are fixed. We see that the appropriate time scale is $(M-1)/(kAU)$. On the time scale of our incompressible problem, $1/(kAU)$, the time interval required for the time-dependent growth rate to reach its asymptotic value (which in this limit coincides with that given by Richtmyer's impulsive formula) tends to zero as $M-1$. Passing to the limit $M-1 \to 0$, we obtain an instantaneous jump of the growth rate to the value predicted by (2.15), as should occur. In figure 1(b) we show a similar transition to the limit of weak compressibility, where we keep $A = 0.55$, $M = 1.5$ fixed and increase $\gamma_1 = \gamma_2 = \gamma$ from 5/3 to 100. We see that the appropriate time scale is $1/(\gamma kAU)$; for the time-dependent growth rate it takes several times $1/\gamma$ of our time unit to reach the same asymptotic value. Passing to the limit $\gamma \to \infty$, we obtain the same instantaneous jump of the growth rate to the velocity predicted by (2.15), as should occur. In the linear approximation the bubble ($x = 0$) and the spike ($x = \pi$) are symmetric in shape, their dimensional vertical velocities are equal to $\pm\varepsilon AU$ (here and below the upper and lower signs refer to bubble and spike, respectively), constant in time and differ only in direction.

The second-order term

$$\xi_1(x, t) = -\tfrac{1}{2}At^2 \cos(2x) \tag{2.16}$$

is the same as in Haan (1991), Zhang & Sohn (1996), Berning & Rubenchik (1998) and Vandenboomgaerde *et al.* (2002); it does not vanish as predicted by Mikaelian (1994). This term describes vertical acceleration, which is constant in time and has the same value $-\varepsilon^2 kA^3U^2$ for the bubble and the spike. Since they move in the opposite directions, this is the lowest-order term to introduce asymmetry between the bubble and the spike: in the second-order the spike always accelerates and the bubble decelerates, see § 2.5 for details.

The third-order term

$$\xi_2(x, t) = \left(\frac{4A^2-1}{8}t^3 - \frac{3}{8}t^2\right)\cos(3x) - \left(\frac{4A^2+1}{24}t^3 + \frac{1}{8}t^2 + \frac{1}{4}t\right)\cos(x) \tag{2.17}$$

is the same as in Zhang & Sohn (1997*b*), Berning & Rubenchik (1998), Zhang & Sohn (1999) and Vandenboomgaerde *et al.* (2002). It differs from the expressions given by Zhang & Sohn (1996, 1997*a*) and Zabusky *et al.* (2003), which coincide with each other. This is the lowest-order term to add nonlinear corrections $\mp\varepsilon^3 AU/4$ to the bubble and spike initial velocities; see § 2.4. It also adds corrections $\mp\varepsilon^3 kA^2U^2$ to the bubble and spike initial accelerations. These corrections, together with the contributions of higher orders, can change the early-time perturbation evolution, making the spike decelerate and the bubble accelerate for the appropriate sign of A and sufficiently large ε; see § 2.5.

The fourth-order term is the same as in Zhang & Sohn (1997*b*) and differs from that given in Zhang & Sohn (1997*a*), Zabusky *et al.* (2003):

$$\xi_3(x, t) = \left(\frac{-2A^2+1}{3}t^4 + \frac{2}{3}t^3 - \frac{1}{4}t^2\right)A\cos(4x) + \left(\frac{A^2}{3}t^4 + \frac{1}{2}t^2 + \frac{1}{12}t\right)A\cos(2x). \tag{2.18}$$

Detailed consideration of the causes of the differences is beyond the scope of the present paper and will be discussed elsewhere. We emphasize that the results presented herein are obtained from the exact solution of the perturbation problem as it is formulated above.

The Fourier coefficient $f_{n,n+1}(t, A)$ of $\cos((n+1)x)$ in the nth term of this expansion, ξ_n, is a polynomial in t of order $n+1$, which includes powers of t starting from two; cf. (2.16)–(2.18). We have obtained an explicit expression for the particular case of a single fluid when $A = \pm 1$:

$$f_{n,n+1}(t, A = \pm 1) = \frac{(n-1)!}{(\pm 2)^n} \sum_{m=2}^{n+1} \frac{(-1)^{m+1}(n+1)^{m-1}}{m!(m-2)!(n-m+1)!} t^m$$
$$= \frac{2L_n[(n+1)t] - L_{n-1}[(n+1)t] - L_{n+1}[(n+1)t]}{(\pm 2)^n (n+1)}, \qquad (2.19)$$

where $L_n(z)$ is a Laguerre polynomial and $n \geqslant 1$. Substituting $A = \pm 1$ into the coefficients of $\cos(2x)$, $\cos(3x)$ and $\cos(4x)$ in (2.16)–(2.18), respectively, we obtain the same expressions as given by substitution of $n = 1$, 2 and 3, respectively, into (2.19).

Formula (2.19) generalizes (6) of Velikovich & Dimonte (1996), where the coefficient at the highest power of t in (2.19), t^{n+1}, is given for $A = +1$. We present here an explicit expression for the coefficient of t^{n+1} in the next Fourier coefficient $f_{n,n-1}$ of $\cos((n-1)x)$ in the nth term of the expansion

$$f_{n,n-1}(t, A = \pm 1) = -\frac{(n-1)^n (3n-1)}{(\mp 2)^n (n+1)!} t^{n+1} + O(t^n), \qquad (2.20)$$

where $n \geqslant 2$. Substituting $A = \pm 1$ into the coefficients of $\cos(x)$ and $\cos(2x)$ in (2.17) and (2.18), respectively, we obtain polynomials in t whose highest-order terms are given by substitution of $n = 2$ and 3, respectively, into (2.20).

2.3. *Bubble and spike amplitudes, velocities and curvatures*

The positions $x = 0$ and $x = \pi$ correspond to the bubble and the spike, respectively. For Atwood number $A > 0$, the bubble of the low-density lower fluid rises and the spike of the high-density upper fluid falls, in the positive and negative y directions, respectively. For $A = 0$ (the so-called Boussinesq approximation: Atwood number $A \to 0$, time $t \to \infty$, the product At being finite) there is full symmetry between the bubble and the spike, one of which rises while the other falls. Finally, for $A < 0$, the bubble of the low-density upper fluid falls and the spike of the high-density lower fluid rises, both experiencing an early-time phase reversal. Substituting $x = 0$ and $x = \pi$ into the expansion (2.14), we obtain the perturbation expansions for the bubble and spike amplitudes:

$$\xi_{b,s}(t) = \pm 1 \pm t - \frac{At^2}{2}\varepsilon \pm \left(\frac{2A^2-1}{6}t^3 - \frac{1}{2}t^2 - \frac{1}{4}t\right)\varepsilon^2$$
$$+ A\left(\frac{-A^2+1}{3}t^4 + \frac{2}{3}t^3 + \frac{1}{4}t^2 + \frac{1}{12}t\right)\varepsilon^3 \pm \left(\frac{92A^4 - 125A^2 + 19}{240}t^5\right.$$
$$\left. + \frac{-37A^2+19}{48}t^4 + \frac{-11A^2+29}{48}t^3 + \frac{-5A^2+19}{48}t^2 + \frac{19}{192}t\right)\varepsilon^4 + \cdots, \qquad (2.21)$$

where the upper and lower signs correspond to the bubble and the spike, respectively.

The bubble and spike velocities are given by

$$U_{b,s}(t) = \frac{\mathrm{d}\xi_{b,s}(t)}{\mathrm{d}t} = \pm 1 - At\varepsilon \pm \left(\frac{2A^2-1}{2}t^2 - t - \frac{1}{4}\right)\varepsilon^2 + A\left(\frac{-4A^2+4}{3}t^3 + 2t^2 + \frac{1}{2}t + \frac{1}{12}\right)\varepsilon^3 \pm \left(\frac{92A^4-125A^2+19}{48}t^4 + \frac{-37A^2+19}{12}t^3 + \frac{-11A^2+29}{16}t^2 + \frac{-5A^2+19}{24}t + \frac{19}{192}\right)\varepsilon^4 + \cdots . \quad (2.22)$$

Similarly, we derive the perturbation expansions for the curvatures of the bubble and the spike at the tip:

$$\frac{1}{kR_{b,s}(t)} = -\left.\frac{\partial^2\xi}{\partial x^2}\right|_{x=0,\pi} = \pm(1+t)\varepsilon - 2At^2\varepsilon^2 \pm \left(\frac{26A^2-7}{6}t^3 - \frac{7}{2}t^2 - \frac{1}{4}t\right)\varepsilon^3 + A\left(\frac{-28A^2+16}{3}t^4 + \frac{32}{3}t^3 - 2t^2 + \frac{1}{3}t\right)\varepsilon^4 \pm \left(\frac{4796A^4-4205A^2+379}{240}t^5 + \frac{-1381A^2+379}{48}t^4 + \frac{277A^2+353}{48}t^3 - \frac{53A^2+5}{48}t^2 - \frac{5}{192}t\right)\varepsilon^5 + \cdots . \quad (2.23)$$

Here, the dimensional values of $R_b > 0$ and $R_s < 0$ are curvature radii of the perturbed interface at the tips of the bubble and the spike, respectively. Their signs are different because, in our notation, the bubble is initially convex and the spike concave. The curvature radii are normalized in (2.23) with respect to the inverse wavenumber k^{-1}.

For a given value of the Atwood number A and the nonlinearity parameter ε the right-hand sides of (2.21)–(2.23) represent Taylor series in normalized time t. The functions generated by these series diverge at large t, but they can be accurately evaluated beyond the circle of convergence, into the moderately nonlinear regime, with the aid of high-order Padé approximations. The behaviour of the bubble can be traced in this way for a longer time than that of the spike. This is because the amplitude of the spike grows faster, leading to mushrooming that starts at some finite instant of time. Starting from this instant of time, the interface is no longer described by a single-valued function $y = \eta(x, t)$, which implies the emergence of a singularity that limits convergence.

To clarify the latter issue, consider any Taylor series in time, such as the series (2.21) for the normalized bubble amplitude:

$$k\eta_b(t) = \varepsilon\xi_b(t) = \varepsilon + \left[1 - \frac{1}{4}\varepsilon^2 + \frac{A}{12}\varepsilon^3 + \frac{19}{192}\varepsilon^4 - \frac{21A}{320}\varepsilon^5 + O(\varepsilon^6)\right]\varepsilon t + \left[-\frac{A}{2} - \frac{1}{2}\varepsilon + \frac{A}{4}\varepsilon^2 + \frac{-5A^2+19}{48}\varepsilon^3 - \frac{13A}{48}\varepsilon^4 + O(\varepsilon^5)\right](\varepsilon t)^2$$

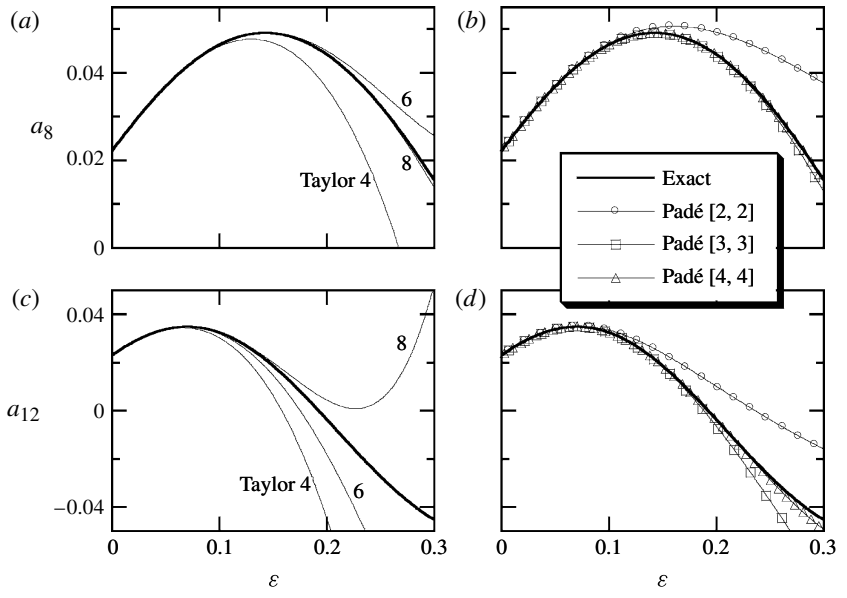

FIGURE 2. Normalized coefficients of the Taylor series (2.23) of the eighth (*a*,*b*) and 12th (*c*,*d*) order. Thick lines show the exact values of the corresponding coefficients vs. ε. Thin solid lines in (*a*) and (*c*) show partial sums of the Taylor series in ε with the first four, six or eight terms retained. Lines with symbols in (*b*) and (*d*) show Padé approximants P_2^2, P_3^3 and P_4^4.

$$+\left[\frac{2A^2-1}{6}+\frac{2A}{3}\varepsilon+\frac{-11A^2+29}{48}\varepsilon^2 + \frac{A(8A^2-53)}{72}\varepsilon^3+O(\varepsilon^4)\right](\varepsilon t)^3+\cdots. \tag{2.24}$$

We see that each coefficient of the Taylor series in t is itself a function of A and ε represented by a Taylor series in ε. If this series in ε converges, then the coefficients of the Taylor series (2.21) (and other similar series, for bubble and spike amplitudes, velocities and curvatures) in time are sufficiently accurately estimated by partial sums of the series, and analytic continuation of the corresponding function of time to larger values of t, beyond its radius of convergence, is entirely possible. It should be noted however that, for evaluating this function at larger values of t, higher-order coefficients of the Taylor series like (2.24) come into play. Further, for any given number N_{max} of terms retained in the perturbation series (2.14), the coefficient of the power t^m contains $N_{max}+2-m$ terms of the Taylor expansion in ε. For smaller ε, a smaller number of terms has to be retained to accurately evaluate the corresponding coefficient of the Taylor series in t. For larger ε, such evaluations could be incorrect even for relatively low-order terms.

To give an example, in figure 2 we plot the eighth and 12th coefficients of the Taylor series (2.24) for $A=0.08$ as functions of the perturbation parameter ε. The series coefficients are normalized to the corresponding powers of ε, i.e. ε^8 and ε^{12}, and denoted by a_8 and a_{12}, respectively. We see that in order to accurately evaluate the eighth coefficient of the Taylor series (2.24) for $\varepsilon=0.1$ we need the terms of expansion (2.14) up to at least the 12th order. To do the same for $\varepsilon=0.2$ we would

need the 16th order. Accurate evaluation of the 12th term up to $\varepsilon = 0.2$ requires calculating the 20th order of the perturbation series. Use of Padé approximation is seen to help, providing more accurate estimates of the Taylor coefficients than direct summation of the available terms of the corresponding expansions in ε. Still, for any finite ε, the coefficients of the Taylor series (2.24) and similar expansions for other variables are approximate, not exact. The approximation is good at small time t, but at some point it inevitably breaks down; the larger the perturbation parameter ε, the earlier this happens. The quality of our analytical approximation is controlled by the convergence of successive higher-order Padé approximants in time.

It must be noted that, since the linear RMI growth rate is of order ε, the dimensionless time when the nonlinear effects become significant is $O(\varepsilon^{-1})$. For very low initial values of ε we can pass to the limit $\varepsilon \to 0$, $t \to \infty$, $\varepsilon t = \tau$ finite, thereby retaining only the leading (i.e. 'the most secular'; cf. Vandenboomgaerde *et al.* (2002)) term in the expansion of each Taylor series coefficient (2.24). Then the number of exact coefficients of the Taylor series (2.24) would be the same as the number of the perturbation series (2.14) terms calculated. The Taylor series expansions in time for RMI in this limit were first introduced by Velikovich & Dimonte (1996) for $A = 1$, and later by Vandenboomgaerde *et al.* (2002) for arbitrary A.

2.4. *Nonlinear correction to the Richtmyer impulsive model*

The most accurate estimates of the perturbation theory refer to the lowest-order terms of the Taylor series like (2.24). For example, substituting $t = 0$ into (2.22), we can derive the initial rate of interfacial growth, and thereby the nonlinear correction C to the initial growth rate estimated by the Richtmyer impulsive model, cf. (2.15) for the bubble and the spike:

$$\begin{aligned} C_{b,s}(\varepsilon, A) \;=\; \left|\frac{\dot\eta_{b,s}(0)}{\dot\eta_{imp}}\right| = |U_{b,s}(0)| = 1 - \frac{1}{4}\varepsilon^2 \pm \frac{1}{12}A\varepsilon^3 + \frac{19}{192}\varepsilon^4 \mp \frac{21}{320}A\varepsilon^5 \\ + \left(\frac{1}{288}A^2 - \frac{167}{3840}\right)\varepsilon^6 \pm \frac{347}{8064}A\varepsilon^7 + \left(-\frac{97}{23\,040}A^2 + \frac{6893}{344\,064}\right)\varepsilon^8 \\ \pm \left(\frac{1}{3456}A^2 - \frac{181\,313}{6635\,520}\right)A\varepsilon^9 + \cdots, \end{aligned} \tag{2.25}$$

where the upper and lower signs correspond to the bubble and the spike, respectively, and

$$\dot\eta_{imp} = kAU\eta_0 = \varepsilon AU \tag{2.26}$$

is the prediction of Richtmyer's linear impulsive model (Richtmyer 1960). As illustrated by (2.12), (2.15)–(2.18), the acceleration pulse does not change the initial Fourier amplitude of the interfacial displacement, which remains single-mode at $t = 0$. However, all the Fourier modes of the velocities of both fluids are instantaneously excited, as follows from the initial conditions (2.12), (2.13). Hence the corrections to the Richtmyer growth rate at $t = 0$ emerge in all orders of ε starting from $O(\varepsilon^2)$. The right-hand side of (2.25) is a function of the Atwood number A and the nonlinearity parameter ε.

Figure 3 shows the correction factors $C_{b,s}$ for the bubble and the spike. The lines represent Padé approximants P^{16}_{16} in ε to the series (2.25), the convergence of which has been checked. We see that the growth rate reduction of the impulsive growth rate

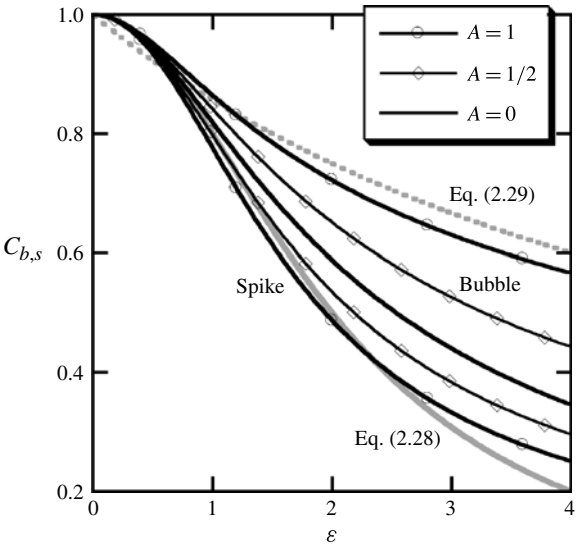

FIGURE 3. The correction factor $C_{b,s}$ generated by the perturbation series (2.25) vs. perturbation parameter ε. Bubble and spike lines, marked by symbols, pass above and below the solid line corresponding to the symmetric case $A = 0$, respectively. For negative Atwood numbers $A < 0$ of the same magnitude $|A| = 1/2$, 1 the labels 'Bubble' and 'Spike' in the figure would swap. Solid and dotted grey lines represent (2.28) and (2.29), respectively.

is greater for the spike than for the bubble if the Atwood number is positive. The bubble-spike symmetry exhibited by (2.25),

$$C_b(A) = C_s(-A), \tag{2.27}$$

ensures that for negative Atwood number this is the other way around. Hence the bubble correction factor for $A = -1$ is the same as the spike correction factor for $A = 1$ and vice versa. The lowest-order correction factor $1 - \varepsilon^2/4$ given by (2.25) is exactly the same for the bubble and the spike and independent of the Atwood number. Neglecting the terms $O(\varepsilon^3)$, which in the exact theory is the lowest order to introduce Atwood number dependence in nonlinear corrections, this factor can be approximated by the formula

$$C_{s,B} = \frac{1}{1 + \varepsilon^2/4}, \tag{2.28}$$

given by Buttler *et al.* (2012) for the spike. These authors also introduced the following expression for the bubble correction:

$$C_{b,B} = \frac{1}{1 + \varepsilon/6}. \tag{2.29}$$

Figure 3 demonstrates that these expressions are close to the exact results for $A = 1$. For the case of $A = -1$ studied experimentally by Buttler *et al.* (2012), the symmetry (2.27) ensures that (2.28) and (2.29) are good approximations for the bubble and spike nonlinear corrections, respectively.

Sometimes it is convenient to use the averaged correction factor

$$C_{av} = \tfrac{1}{2}(C_b + C_s). \tag{2.30}$$

Expansion of $C_{av}(\varepsilon, A)$, which obviously contains only even powers of ε in (2.25), is the same as published previously by Holmes *et al.* (1999).

It turns out that an explicit expression for the correction factor (2.25) can be obtained for the limiting case of $A = 0$, which corresponds to the Boussinesq approximation:

$$C(\varepsilon, A = 0) = \frac{2}{\varepsilon} \sum_{n=1}^{\infty} \mathrm{I}_n(n\varepsilon) \exp(-n\varepsilon), \tag{2.31}$$

where $\mathrm{I}_n(z)$ is the modified Bessel function (we have omitted the subscript of C because, for $A = 0$, obviously $C_b = C_s = C_{av}$ for any ε). The nth term in the series (2.31) is the contribution of the corresponding Fourier harmonic, $\cos(nx)$, its coefficient being the result of summation of all orders of the perturbation series in ε. This result therefore applies to the strongly nonlinear case of $\varepsilon \gg 1$ as well as to the weakly and moderately nonlinear cases of $\varepsilon < 1$. For arbitrary positive ε the series (2.31) converges absolutely, making it possible to directly evaluate the correction factor for any ε. The Taylor series in ε for the same function has a finite radius of convergence. Its asymptotic behaviour in the limits of weak and strong nonlinearity is found directly from (2.25), (2.31):

$$C(\varepsilon, A = 0) = \begin{cases} 1 - \dfrac{1}{4}\varepsilon^2 + \dfrac{19}{192}\varepsilon^4 + O(\varepsilon^6), & \varepsilon \ll 1, \\ \dfrac{2}{\varepsilon} + \sqrt{\dfrac{2}{\pi}} \dfrac{\zeta(1/2)}{\varepsilon^{3/2}} + O\left(\dfrac{1}{\varepsilon^2}\right), & \varepsilon \gg 1, \end{cases} \tag{2.32}$$

where $\zeta(z)$ is the Riemann zeta function. For large ε high Fourier modes dominate in the correction to the growth rate; indeed the contribution of low-order terms to (2.32) is $O(\varepsilon^{-3/2})$.

Figure 4 demonstrates evaluation of the function $C_{av}(\varepsilon, A)$ generated by the series (2.25), (2.30), together with the exact expression (2.31) and its asymptotic approximations (2.32) for $A = 0$. Since the expansion (2.25) for the averaged correction factor (2.30) contains only even powers of A, the results of figure 4 apply to any sign of A for given $|A|$. In figure 4(*a*), plotted for $|A| = 1$, we compare evaluation via direct summation with analytic continuation using Padé approximation. Within the circle of convergence of the series (2.25), for $\varepsilon < 1$, direct summation works fine, and all methods of evaluation yield the same result. For $\varepsilon > 1$ direct summation does not work. On the other hand, the high-order Padé approximants are seen to converge with increasing order, generating a well-defined function of ε for a given $|A|$.

Since in the expansion (2.25), (2.30) only the terms starting from $O(\varepsilon^6)$ depend on A, the function $C_{av}(\varepsilon, A)$ is weakly dependent on the Atwood number A, as demonstrated by figure 4(*b*), where the correction factors C_{av} are plotted vs. ε for $|A|$ ranging from zero to one. The small-ε and large-ε asymptotic expressions with the terms retained in (2.32) are seen to provide a fairly good approximation for $A = 0$ at $\varepsilon < 1$ and $\varepsilon > 1$, respectively. These expressions are seen to approximate $C_{av}(\varepsilon, A)$ for $|A| < 1/2$ sufficiently well in the whole range of ε shown in figure 3. For comparison,

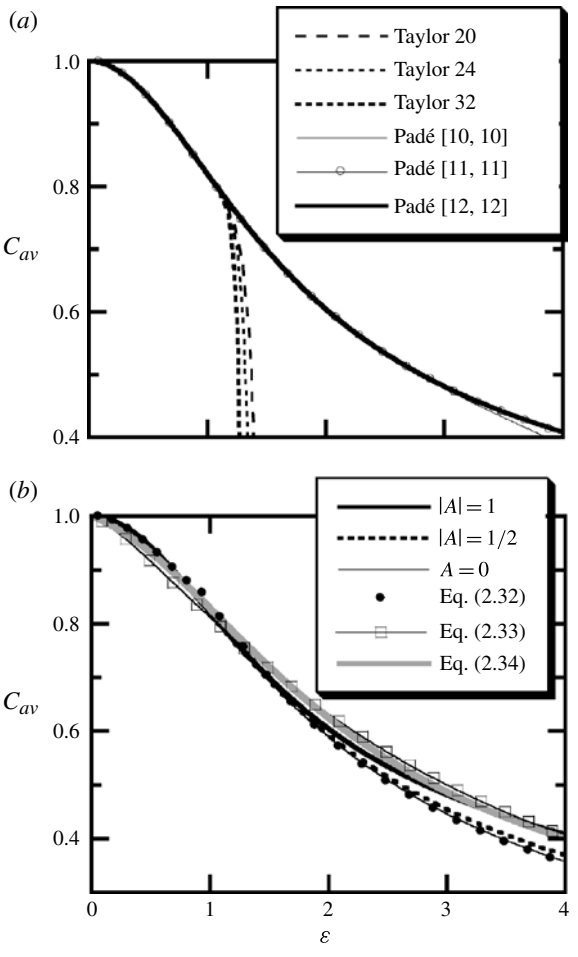

FIGURE 4. The averaged correction factor C_{av} generated by the perturbation series (2.25), (2.28) vs. perturbation parameter ε: (*a*) partial sums of the series retaining its first 20, 24 and 32 terms compared to the Padé approximants P_{10}^{10}, P_{11}^{11} and P_{12}^{12} for $|A| = 1$. (*b*) C_{av} vs. ε for $|A| = 1$, $1/2$ and 0 compared to the asymptotic formula (2.32) (upper line for $\varepsilon < 1$, lower line for $\varepsilon > 1$, filled circles) and approximate formulas (2.33) from Dimonte & Ramaprabhu (2010) (empty boxes) and (2.34) (solid grey line).

in figure 4(*b*) we present two approximate interpolation formulas. One is given by Dimonte & Ramaprabhu (2010):

$$C_{av,DR}(\varepsilon) = \frac{1}{1 + (\varepsilon/3)^{4/3}}. \tag{2.33}$$

The other is obtained by substituting the approximations (2.28) and (2.29) into (2.30):

$$C_{av,B}(\varepsilon) = \frac{24 + 2\varepsilon + 3\varepsilon^2}{(6 + \varepsilon)(4 + \varepsilon^2)}. \tag{2.34}$$

In the range $\varepsilon \leqslant 4$ these functions are seen to be very close to each other, deviating from the exact values of $C_{av}(\varepsilon, A)$ by less than 10 % for any A. It appears that for

arbitrary A the exact correction factor $C_{av}(\varepsilon, A)$ does not decrease with increasing ε faster that $2/\varepsilon$, the exact asymptotic law obtained for $A = 0$. The function (2.34) decays at large ε proportionally to the same power of $1/\varepsilon$ as the exact formula (2.31). On the other hand, (2.33) is seen to decay faster than $1/\varepsilon$ for large ε, so the discrepancy between (2.33) and the exact result is expected to increase for large ε.

Reduction of the peak RM growth rate due to finite initial amplitude given by $C_{av}(\varepsilon, A)$ has been found to be in reasonable agreement with experimental data (Velikovich & Dimonte 1996; Glendinning *et al.* 2003) and numerical simulation results (Holmes *et al.* 1999; Dimonte & Ramaprabhu 2010; Stanic *et al.* 2012).

2.5. *Early-time spike and bubble acceleration*

Another interesting feature of the nonlinear RM growth, which is determined by the low-order terms in the Taylor expansion in time, is the difference in the early-time dynamics of the bubble and the spike. For $A > 0$ the bubble decelerates from the very beginning, whereas the spike can accelerate for some time before its acceleration changes sign and it starts slowing down. This property of RMI at $0 < A < 1$ was first discovered by Neuvazhaev & Parshukov (1992) and later confirmed by Sadot *et al.* (1998), Dhotre, Ramaprabhu & Dimonte (2008). As stated by Neuvazhaev & Parshukov (1992), the spike velocity 'starts decreasing at once for large initial amplitudes ($\varepsilon = 0.5$), while for small amplitudes there is a short time interval in which the "spike" velocity is increasing before starting to decrease, i.e. the "spike" behaviour depends on the initial perturbation amplitude ε. Therefore there arises a supposition that for the given Atwood number there is a critical value of the initial amplitude ε_{cr}, such as that if $\varepsilon > \varepsilon_{cr}$, then the "spike" velocity is decreasing at once, and if $\varepsilon < \varepsilon_{cr}$, then there is a short period of the "spike" velocity growth' (here we have replaced their original notation with ours). The critical values ε_{cr} determined by Neuvazhaev & Parshukov (1992) for $A = 0.1$, 0.33 and 0.8 are 0.1, 0.34, and 1.04, respectively (note that the sign of the Atwood number A as defined by Neuvazhaev & Parshukov (1992) is opposite to ours).

Various model formulas developed to approximate the RM spike and bubble dynamics, which are summarized by Dimonte & Ramaprabhu (2010), can be used to formulate the conditions for early-time spike and bubble acceleration. The empirical model of Zhang & Sohn (1996, 1997*a*) (see also (2.14) in Dimonte & Ramaprabhu (2010)), predicts early-time spike acceleration for $A > 0$ if

$$A > \varepsilon. \tag{2.35}$$

According to the model of Sadot *et al.* (1998) (see also (2.22) in Dimonte & Ramaprabhu (2010)), the spike accelerates at early time for any combination of ε and A, whereas the bubble never does. Finally, the empirical model developed by Dimonte & Ramaprabhu (2010) and expressed by their equations (2.24, 2.25) predicts early-time spike acceleration for

$$A > A_{cr,DR}(\varepsilon) = \frac{4\varepsilon + 1}{2(5 - \varepsilon)} \tag{2.36}$$

and no early-time bubble acceleration.

Perturbation theory makes it possible to determine exactly the parameter ranges in the (ε, A) plane corresponding to early-time spike and bubble acceleration, or absence thereof. For this purpose, differentiating (2.22) with respect to time and substituting

$t=0$ into the result, we can derive perturbation expansions for the initial normalized acceleration of the bubble and the spike:

$$\begin{aligned} a_{b,s}(0) &= \frac{1}{\varepsilon}\times\left.\frac{\mathrm{d}U_{b,s}}{\mathrm{d}t}\right|_{t=0} = \frac{1}{\varepsilon}\times\left.\frac{\mathrm{d}^2\xi_{b,s}}{\mathrm{d}t^2}\right|_{t=0} \\ &= -A\mp\varepsilon+\frac{A}{2}\varepsilon^2\mp\left(\frac{5A^2-19}{24}\right)\varepsilon^3-\frac{13A}{24}\varepsilon^4\pm\left(\frac{101A^2}{480}-\frac{177}{320}\right)\varepsilon^5 \\ &\quad +O(\varepsilon^6). \end{aligned} \tag{2.37}$$

The vertical bubble velocity has the same sign as the Atwood number: the bubble of the light fluid rises in the positive y direction if $A>0$ and falls in the negative y direction if $A<0$. Conversely, the sign of the vertical spike velocity is opposite to that of the Atwood number: the spike of the heavy fluid falls in the negative y direction if $A>0$ and rises in the positive y direction if $A<0$. We conclude that the bubble accelerates if the right-hand side of (2.37) has the same sign as the Atwood number A, whereas the spike accelerates when its sign is opposite to that of A.

The lowest-order term in the expansion (2.37) comes from the second-order term (2.16) in our perturbation expansion. The sign of this term indicates that for any $A\neq 0$ and sufficiently small ε the spike always accelerates and the bubble always decelerates at early time. Higher-order corrections in ε can change the sign of the right-hand side of (2.37), making the spike decelerate and the bubble accelerate at early time. Retaining the next-order terms in (2.37) that come from (2.17), we find that such behaviour is predicted at $A>0$ for the spike and at $A<0$ for the bubble provided that $|A|<\varepsilon$. For spike acceleration this is consistent with (2.35) because the model of Zhang & Sohn (1996, 1997*a*) is based on a similar perturbation expansion, and the terms contributing to (2.35) are exactly the same as those in (2.16), (2.17).

For arbitrary ε, the parameter ranges in the (ε, A) plane that correspond to the early-time acceleration and deceleration of the bubble and the spike are separated by the lines found from the equations

$$a_{b,s}(0)=0. \tag{2.38}$$

Solving (2.38) for A, we obtain the conditions for early-time spike and bubble acceleration involving a function generated by its Taylor series in ε. For positive Atwood number, $A>0$, the spike is predicted to accelerate at early time if

$$A>A_{cr}(\varepsilon)=\varepsilon-\tfrac{7}{24}\varepsilon^3+\tfrac{71}{960}\varepsilon^5+\tfrac{619}{107\,520}\varepsilon^7-\tfrac{1518\,899}{46\,448\,640}\varepsilon^9+O(\varepsilon^{11}), \tag{2.39}$$

and the bubble accelerates if $A<-A_{cr}(\varepsilon)$. For negative Atwood number $A<0$ the conditions for early-time spike and bubble acceleration are opposite: $A<A_{cr}(\varepsilon)$ and $A>-A_{cr}(\varepsilon)$, respectively.

The series in the right-hand side of (2.39) converges for $\varepsilon<1$, generating an analytic function $A_{cr}(\varepsilon)$. It can be analytically continued beyond $\varepsilon=1$ using Padé approximation. We found this function to be positive: $A_{cr}(\varepsilon)>0$ for $\varepsilon>0$. Therefore the condition for early-time spike acceleration is not satisfied only for positive Atwood number at $0<A<A_{cr}(\varepsilon)$. Conversely, the condition for early-time bubble acceleration is satisfied only for negative Atwood number at $-A_{cr}(\varepsilon)<A<0$.

Approximating $A_{cr}(\varepsilon)$ we find that the error of the fifth-order Padé approximant P_2^3 is smaller than 1 % at $\varepsilon\leqslant 1$. The corresponding approximate expression for the function $A_{cr}(\varepsilon)$ is

$$\tilde{A}_{cr}(\varepsilon)=\frac{8\varepsilon(105-4\varepsilon^2)}{3(280+71\varepsilon^2)}. \tag{2.40}$$

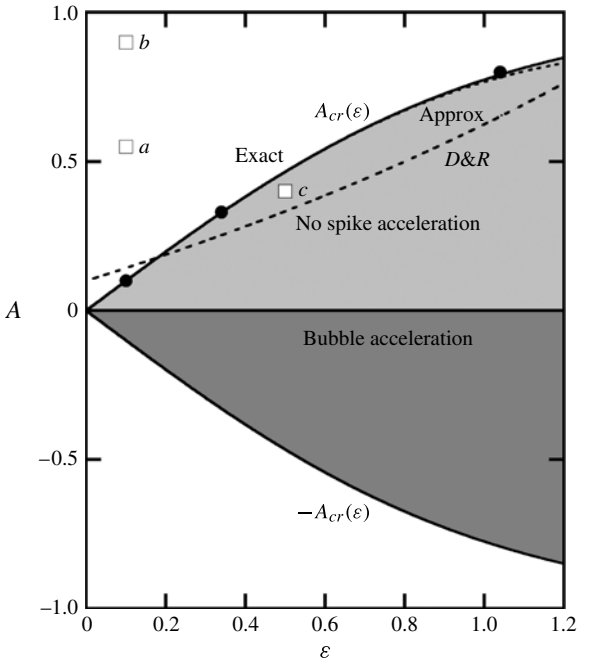

FIGURE 5. Shaded regions are parameter ranges in the plane (ε, A) corresponding to the absence of early time spike acceleration and the presence of early-time bubble acceleration. The solid line is the exact result of perturbation theory; the dotted line is the approximation (2.39); the dashed line labelled D&R is the approximate formula (36) from Dimonte & Ramaprabhu (2010); filled circles are results of Neuvazhaev & Parshukov (1992). Empty boxes correspond to the conditions of our simulations: for points a ($\varepsilon = 0.1$, $A = 0.55$) and b ($\varepsilon = 0.1$, $A = 0.9$) spike acceleration is predicted; for point c ($\varepsilon = 0.5$, $A = 0.4$) no spike acceleration is predicted by the perturbation theory.

Figure 5 shows the parameter ranges in the plane (ε, A) corresponding to the presence or absence of early-time spike and bubble acceleration. The light grey shaded region between the solid line $A = A_{cr}(\varepsilon)$ and the horizontal axis $A = 0$ corresponds to the absence of early-time spike acceleration. Outside this region in the plane (ε, A) the spike accelerates at early time. The dark grey shaded region between the solid line $A = -A_{cr}(\varepsilon)$ and the horizontal axis $A = 0$ corresponds to early-time bubble acceleration. Outside this region in the plane (ε, A) the bubble decelerates at all times. The solid line is the exact result of the perturbation theory stemming from (2.39) (that is, the Padé approximant P_4^5, convergence of which has been checked), the dotted line is the lower-order approximation (2.40), the dashed line labelled D&R is the right-hand side of approximate formula (36) of Dimonte & Ramaprabhu (2010). The symbols correspond to the conditions of our simulations described in § 4. For points a ($\varepsilon = 0.1$, $A = 0.55$) and b ($\varepsilon = 0.1$, $A = 0.9$) early-time spike acceleration is predicted by all models. Point c has been chosen in the domain where the predictions differ: early-time spike acceleration is predicted for $\varepsilon = 0.5$, $A = 0.4$ by the Dimonte & Ramaprabhu (2010) and Sadot *et al.* (1998) models, but not by the perturbation theory. Capturing the difference between these predictions (see § 4) is a very demanding verification test for a simulation code.

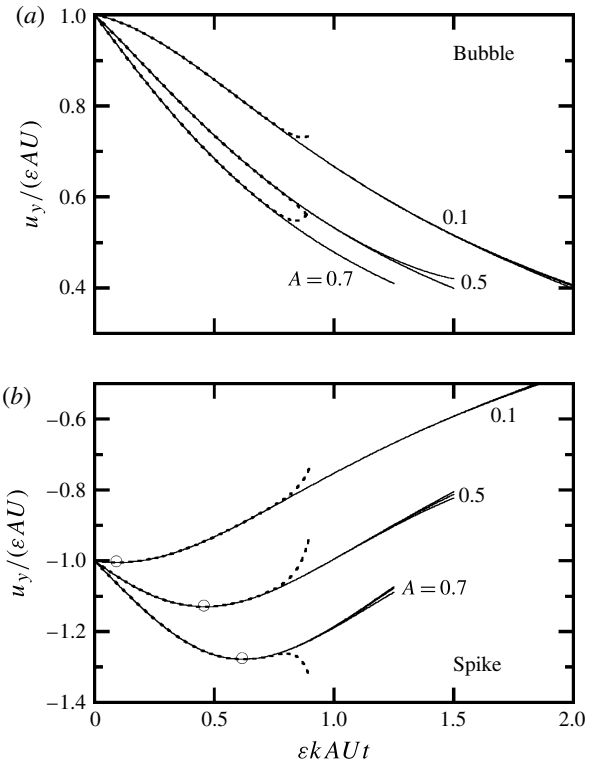

FIGURE 6. Time histories of normalized bubble and spike velocities for $\varepsilon = 0.005$ and the Atwood number A values indicated. Dotted lines show the results of direct summation of the respective Taylor series in time, thin solid lines – Padé approximants to this series, P_6^6, P_8^8 and P_{10}^{10}. The symbols mark the start of spike deceleration.

Solving (2.38) for ε, we find the critical value of $\varepsilon = \varepsilon_{cr}(A)$ as a function of the Atwood number A. For $A = 0.1$, 0.33 and 0.8, we obtain $\varepsilon_{cr} = 0.100$, 0.341 and 1.061, respectively, in excellent agreement with Neuvazhaev & Parshukov (1992), whose results are shown in figure 5 as filled circles. These authors observed spike acceleration but no bubble acceleration for both single-fluid cases of $A = 1$ and $A = -1$ at $\varepsilon \leqslant 0.5$, which is also consistent with our figure 5 (note that in their figure 3, showing the time histories of bubble and spike velocities, the 'bubble' and 'spike' labels are misplaced).

For small ε we find the following explicit estimate for the dimensional time $t = t_{b,s}$ when the bubble or spike velocity reaches its peak and its deceleration starts:

$$kAUt_{b,s} \cong \mp\frac{A}{\varepsilon} - 1. \tag{2.41}$$

It is applicable for either sign of the Atwood number A. Higher-order terms in ε and A add corrections to this simple formula.

Figure 6 shows the time histories of bubble and spike velocities calculated for very low $\varepsilon = 0.005$ and Atwood number values $A = 0.1$, 0.5 and 0.7, as in figure 6 of the theoretical paper by Volkov *et al.* (2003). Here the time scale $1/(\varepsilon kAU)$ and velocity scale εAU are the same as in Volkov *et al.* (2003), although their choice

of velocity signs is different: negative for the bubble, positive for spike. The dotted lines in figure 6 represent direct summation of the corresponding Taylor series, while the solid lines represent Padé approximants P_6^6, P_8^8 and P_{10}^{10} in t extending the range of convergence. For all the combinations of ε and A in figure 6 early-time spike acceleration is predicted. The instant of peak spike velocity (which for all cases is in the range of convergence of the original Taylor series in time) is estimated by (2.41) with relative errors of 0.33 %, 7.6 % and 12 %, for $A = 0.1$, 0.5 and 0.7, respectively. We find qualitative, but not quantitative agreement with the time histories of spike velocities shown in figure 6 of Volkov *et al.* (2003). Their time histories look different for all cases, the instants of the respective velocity peaks are shifted and the peak spike velocities are different: e.g. their peak spike velocity in the case of $A = 0.7$ is close to -1.5, whereas our estimate for this case is -1.278, as shown in figure 6.

Since the incompressible RMI problem solved here and in Volkov *et al.* (2003) is identical, the above discrepancy could be caused by insufficient numerical accuracy of the calculation in Volkov *et al.* (2003), or by problems with their analytical approach. These authors also show the discrepancy between their results and those obtained for the same problem with the vortex method of Neuvazhaev & Parshukov (1992), whose results are in excellent agreement with ours. Analysis of the cause of this discrepancy is beyond the scope of the present paper. We would like only to emphasize here the importance of exact theoretical results obtained without any numerical approximation, entirely by algebraic manipulations, and therefore suitable for the verification of other theoretical approaches.

2.6. *Velocity profiles*

The solution delivered by perturbation theory can be used to construct velocity profiles in both fluids. The normalized velocity potentials (2.6) can be expressed as Fourier series

$$\phi_{1,2}(x, y, t, \varepsilon, A) = \sum_{n=1}^{\infty} \varphi_{1,2}^{(n)}(t, \varepsilon, A) \exp(\pm ny) \cos(nx), \tag{2.42}$$

where the coefficients are

$$\left.\begin{aligned}
\varphi_{1,2}^{(1)}(t, \varepsilon, A) &= \pm 1 + \left[\pm\frac{1}{8} + \frac{A \pm 1}{2} \mp \frac{(A \mp 1)(2A \pm 1)}{4} t^2\right] \varepsilon^2 + O(\varepsilon^4); \\
\varphi_{1,2}^{(2)}(t, \varepsilon, A) &= \varepsilon \left[-\frac{1}{2} \mp \frac{A \pm 1}{2} t + O(\varepsilon^2)\right]; \\
\varphi_{1,2}^{(3)}(t, \varepsilon, A) &= \varepsilon^2 \left[\pm\frac{3}{8} + \frac{A \pm 1}{2} t \pm \frac{(A \pm 1)(2A \pm 1)}{4} t^2 + O(\varepsilon^2)\right]; \ldots
\end{aligned}\right\} \tag{2.43}$$

and the upper and lower signs correspond to the lower and upper fluids, 1 and 2, respectively.

We see that each of the coefficients of the Fourier expansion (2.42) represents a Taylor series in both the perturbation parameter ε and time t, whose coefficients, in turn, depend on the Atwood number A. For a particular case discussed in § 2.4, explicit summation of the perturbation series over ε can be done at $t = 0$, resulting in

$$\varphi_{1,2}^{(n)}(t = 0, \varepsilon, A = 0) = -\frac{2(\mp 1)^n}{n\varepsilon} \mathrm{I}_n(n\varepsilon). \tag{2.44}$$

Substituting (2.44) into (2.42), we exactly determine the velocity field at $t = 0$ in the whole space.

From this, equation (2.31) is immediately derived.

We are interested in the time-dependent profiles of vertical and horizontal velocities, u_y and u_x. These will be shown below vs. the normalized vertical coordinate ky for specific values of the horizontal coordinate, which correspond to bubble position $x = 0$, spike position $kx = \pi$ and halfway between these two positions, at $kx = \pi/2$. The expansions (2.42) of the velocity potentials $\phi_{1,2}(x, y, t, \varepsilon, A)$ can be regarded as Taylor series in the variable $z = \exp(\pm y)$, where the plus and minus signs correspond to the lower and upper fluids, respectively. The coefficients of the series are functions of t, ε and A which, in turn, are represented by Taylor series in these variables. If ε is sufficiently small, then the series in ε converge for $t < \varepsilon^{-1}$ and the coefficients of the series in z can be accurately evaluated by direct summation (of course, convergence in each case should be checked separately). But the variable z, which by definition is small far from the interface, can approach and even exceed unity in the vicinity of the interface (e.g. for the lower fluid at bubble position $x = 0$, where the tip of the bubble is located at $y = k\eta_b > 0$, so that $z = \exp(k\eta_b) > 1$). Here again, one needs to analytically continue the functions of z (and thereby y) generated by the Taylor series that converge at small z, far from the interface, to the vicinity of the interface, with the aid of high-order Padé approximation.

Figure 7 shows the theoretical profiles of normalized vertical velocity $u_y/(AU)$ calculated for bubble position $x = 0$ with $\varepsilon = 0.1$ and Atwood number A decreasing from 0.9 (a) to 0.55 (b) to $A \to 0$ (c). In the latter case, velocity normalization $u_y/(AU)$ is also understood as the Boussinesq limit of this ratio, since the vertical velocity is also as small as A. The profiles are shown for the range $-2 \leqslant ky \leqslant 2$. Beyond this range the first Fourier mode in the expansion (2.42) is seen to dominate because its decay with distance from the bubble tip is slowest. Far from the interface the vertical velocity decays exponentially as $\exp(\pm ky)$ in the light and heavy fluid, respectively.

The sharp peaks of the velocity profiles in figure 7 correspond to the positions of the bubble tip, $y = \eta_b(t)$. The vertical coordinate of the peak is the bubble velocity, $u_y = U_b(t)$, at the given instant of time. We see that at the bubble position $x = 0$ both light and heavy fluids rise with the bubble. As the perturbation expands into a larger volume, the velocities of both fluids decrease in different ways. In the light fluid, velocity decreases with time at any given vertical position y close to the bubble tip. In the light fluid, the velocity profile appears to flatten with time near the tip: its peak value at the tip of the bubble decreases, whereas its value far from the tip slightly increases, which is more pronounced for larger values of the Atwood number A and at later time. The velocity of the heavy fluid is seen to increase with time at any given vertical position y for $A = 0$, exceeding the velocity at this position y at $t = 0$; see figure 7(c). For an intermediate value of $A = 0.55$ in figure 7(b), the velocity increases with time for y close to the initial position of the bubble tip for some time, and then starts to decrease, eventually going below the velocity at this position y at $t = 0$. For a large value of $A = 0.9$, the period of acceleration is so short that it is not seen in figure 7(a). Consistent with the results shown in figure 6(a), the bubble moves faster and decelerates slower for lower Atwood number A, in agreement with Volkov *et al.* (2003), Abarzhi (2008) and Herrmann *et al.* (2008).

Figure 8 shows the theoretical profiles of the normalized vertical velocity $u_y/(AU)$ calculated for the spike position $kx = \pi$, all the other parameters being the same as in figure 7. Here, the sharp peaks of the velocity profiles correspond to the positions of the spike tip $y = \eta_s(t)$ and the vertical coordinate of the peak is the spike velocity $u_y = U_s(t)$ at the given instant of time. Both light and heavy fluids are seen to fall

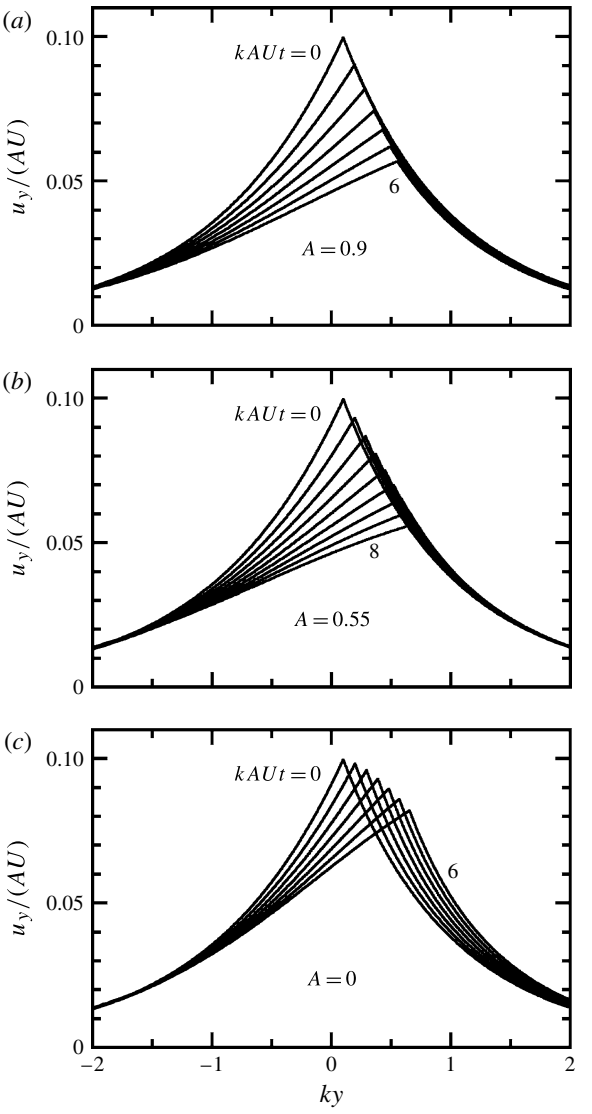

FIGURE 7. Theoretical time-dependent profiles of normalized vertical velocity at bubble position $x = 0$ for $\varepsilon = 0.1$: (*a*) $A = 0.9$; (*b*) $A = 0.55$; (*c*) $A \to 0$ shown starting at $t = 0$ with time increment $\Delta(kAUt) = 1$ from left to right.

with the spike. For large Atwood number $A = 0.9$, figure 8(*a*), the spike is seen to accelerate during the whole time interval up to $kAUt = 5$; the acceleration is predicted by (2.41) to end only at $kAUt \approx 8$. For $A = 0.55$ the spike acceleration is predicted to end at $kAUt \approx 4.5$, which is consistent with figure 8(*b*). Finally, for $A = 0$ the spike starts decelerating from the beginning. Otherwise the velocity profiles are similar for all values of the Atwood number. In the light fluid, the velocity at any given vertical position y increases until the spike passes it. The velocity of the heavy fluid at any given y decreases with time. Due to the symmetry between the light and heavy fluids in the limit $A \to 0$, the velocity profiles in figure 8(*c*) are exactly the same as in

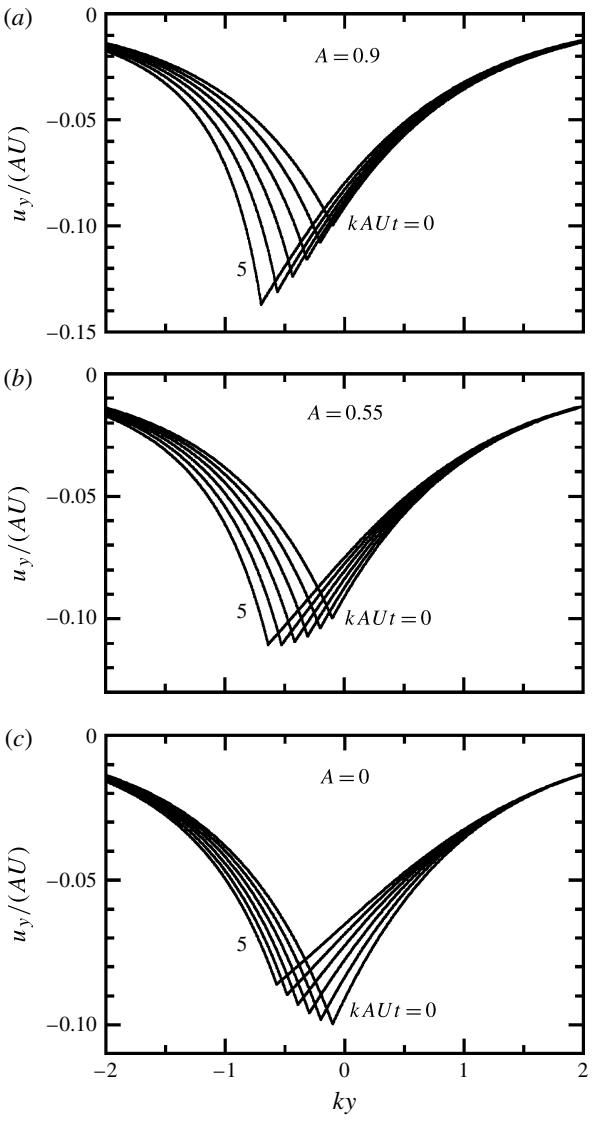

FIGURE 8. Theoretical time-dependent profiles of normalized vertical velocity at spike position $kx = \pi$ for $\varepsilon = 0.1$: (*a*) $A = 0.9$; (*b*) $A = 0.55$; (*c*) $A \to 0$ shown starting at $t = 0$ with time increment $\Delta(kAUt) = 1$ from right to left.

figure 7(*c*), only with inverted sign of velocity and thereby direction of propagation. The spike in figure 8(*c*) decelerates exactly as the bubble in figure 7(*c*).

Figure 9 shows the profile of the normalized horizontal velocity $u_x/(AU)$ halfway between spike and bubble positions, at $kx = \pi/2$, all other conditions being the same as in figures 7, 8. The discontinuity in the horizontal velocity corresponds to the position of the material interface, where the tangential velocity is discontinuous. The profile of the horizontal velocity appears to flatten with time in both fluids near the interface. The flattening is seen to proceed somewhat more quickly in the lighter fluid for large and moderate values of the Atwood number, $A = 0.9$ and 0.55; see figure 9(*a*,*b*). In the limit $A \to 0$ of figure 9(*c*), there is no vertical motion of the

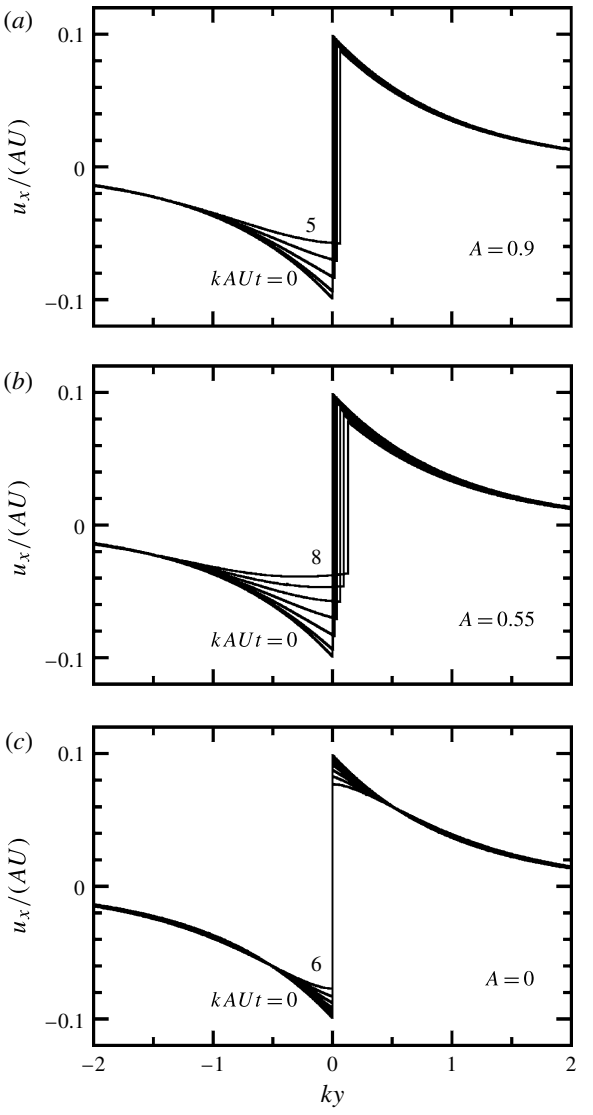

FIGURE 9. Theoretical time-dependent profiles of normalized horizontal velocity halfway between bubble and spike positions, at $kx = \pi/2$, for $\varepsilon = 0.1$: (*a*) $A = 0.9$; (*b*) $A = 0.55$; (*c*) $A \to 0$ shown starting at $t = 0$ with time increment $\Delta(kAUt) = 1$ from bottom to top at $y < 0$.

material interface at $kx = \pi/2$. There is full symmetry between the two fluids and the flattening near the interface proceeds at the same rate in both.

3. Numerical modelling

3.1. *Governing equations*

In our numerical simulations, we solve the unsteady 2D Navier–Stokes equations for immiscible fluids in the incompressible limit,

$$\frac{\partial \boldsymbol{u}}{\partial t} + \boldsymbol{u} \cdot \nabla \boldsymbol{u} = -\frac{1}{\rho}\nabla p + \frac{1}{\rho}\nabla \cdot (\mu(\nabla \boldsymbol{u} + \nabla^{\mathrm{T}}\boldsymbol{u})) + \boldsymbol{g} + \frac{1}{\rho}\boldsymbol{T}_{\sigma}. \tag{3.1}$$

Here $\boldsymbol{g}$ is the time dependent acceleration vector and $\boldsymbol{T}_\sigma$ is the surface tension force, which is non-zero only at the location of the immiscible interface $\boldsymbol{x}_f$:

$$\boldsymbol{T}_\sigma(\boldsymbol{x}) = \sigma\kappa\delta(\boldsymbol{x}-\boldsymbol{x}_f)\boldsymbol{n}, \tag{3.2}$$

with σ an assumed constant surface tension coefficient, κ the local mean interface curvature, $\boldsymbol{n}$ is the local interface normal, and δ the delta function. The continuity equation results in a divergence-free constraint on the velocity field:

$$\nabla\cdot\boldsymbol{u} = 0. \tag{3.3}$$

We describe the location and motion of the interface separating the two immiscible fluids by a level set approach, defining the level set scalar G to be zero at the location of the interface and a signed distance function away from the interface. This results in the level set advection equation

$$\frac{\partial G}{\partial t} + \boldsymbol{u}\cdot\nabla G = 0. \tag{3.4}$$

We assume the density and viscosity to be constant in each fluid, hence their local values can be calculated as a function of the level set scalar using

$$\left.\begin{aligned}\rho(\boldsymbol{x}) &= H(G)\rho_1 + [1-H(G)]\rho_2;\\ \mu(\boldsymbol{x}) &= H(G)\mu_1 + [1-H(G)]\mu_2,\end{aligned}\right\} \tag{3.5}$$

where the indices 1 and 2 denote values in the two fluids and H is the Heaviside function. The interface normal and curvature are calculated from the level set scalar using

$$\boldsymbol{n} = \frac{\nabla G}{|\nabla G|}, \quad \kappa = \nabla\cdot\boldsymbol{n}. \tag{3.6a,b}$$

3.2. *Numerical methods*

The governing equations summarized in the previous section are solved using the flow solver NGA (Desjardins *et al.* 2008), coupled to the level set based interface solver LIT (Herrmann 2008). The flow solver uses a single fluid, fractional step, second-order finite volume formulation on a staggered mesh. The pressure is a Lagrange multiplier and is calculated from a Poisson equation with the subsequent projection step of the predicted velocities enforcing the divergence-free constraint (3.3); see Herrmann (2008). The control volume density and viscosity are calculated from a control volume volume fraction ψ_{cv},

$$\left.\begin{aligned}\rho_{cv} &= \psi_{cv}\rho_1 + (1-\psi_{cv})\rho_2;\\ \mu_{cv} &= \psi_{cv}\mu_1 + (1-\psi_{cv})\mu_2,\end{aligned}\right\} \tag{3.7}$$

where

$$\psi_{cv} = \frac{1}{V_{cv}}\int_{V_{cv}} H(G)\mathrm{d}V \tag{3.8}$$

is integrated over the flow solver control volume V_{cv}.

The level set solver solves all level set related equations on an overset, equidistant Cartesian mesh using a dual-narrow band approach for efficiency (Herrmann 2008). Thus, the integral for the flow solver volume fraction in the above equation is evaluated using the level set grid data as

$$\frac{1}{V_{cv}}\int_{V_{cv}} H(G)\mathrm{d}V = \frac{\sum_{i_G} V_{cv,i_G}\psi_{i_G}}{\sum_{i_G} V_{cv,i_G}}, \tag{3.9}$$

where ψ_{i_G} is evaluated using the analytical volume fraction formula developed by Van der Pijl *et al.* (2005), and V_{cv,i_G} is the intersection volume between the flow solver control volume and the level set grid cell i_G.

The surface tension term in the Navier–Stokes equations, required at the cell faces f, is calculated using the continuum surface force approach (Brackbill, Kothe & Zemach 1992) as

$$(\boldsymbol{T}_\sigma)_f = \sigma\kappa_f(\boldsymbol{\nabla}\psi_{cv})_f. \tag{3.10}$$

Here the gradient of the volume fraction is evaluated using simple central differences to the cell faces, and the cell face curvature is determined by an arithmetic average over control volumes sharing the face and that contain part of the immiscible interface, i.e. have volume fractions larger than zero and smaller than one. The control volume curvature is calculated using the level set grid solution as

$$\kappa_{cv} = \frac{\sum_{i_G} V_{cv,i_G}\delta_{i_G}\kappa_{i_G}}{\sum_{i_G} V_{cv,i_G}\delta_{i_G}}, \tag{3.11}$$

where δ_{i_G} is one if the level set grid cell i_G contains part of the immiscible interface and zero otherwise, and the level set grid curvature, κ_{i_G} is calculated with second-order central differences, using an interface projected approach, to obtain second-order accurate curvatures of the immiscible interface itself (Herrmann 2008).

In LIT, the level set advection equation and the reinitialization partial differential equation to maintain G as a signed distance function (Sussman, Smereka & Osher 1994; Peng *et al.* 1999) are solved using a fifth-order WENO scheme (Jiang & Peng 2000) combined with a third-order Runge–Kutta TVD method (Shu 1988). Further details concerning the numerical methods used, as well as verification test cases and applications demonstrating the performance of the method can be found in Herrmann (2008, 2010).

It should be pointed out that although our approach conserves mass, momentum, and kinetic energy discretely within each fluid, overall conservation depends on the accuracy of the level set interface capturing method. Pure level set methods, as used here, are not discretely volume/mass conserving, thus any error in interface position can translate into a local mass, momentum, and kinetic energy error. Thus, these quantities are conserved only up to the error and order of the employed level set advection/reinitialization scheme. However, after grid refinement, these errors disappear making solution verification indispensable.

3.3. *Computational set-up*

Simulations are performed in a box of aspect ratio four using a single wave of wavelength $\lambda = 1$. The initial disturbance is accelerated by a top-hat acceleration pulse of non-dimensional duration $\Delta t_g = 10^{-4}$ time units and non-dimensional acceleration $g = 10^4$. Simulations have been performed to confirm that neither the choice of computational domain size, nor the pulse duration for constant $U = g\Delta t_g$ change the reported results in a significant way. Thus our reported results are not influenced by the choice of our regularization for (2.3).

Equidistant Cartesian meshes were used both for the flow solver and the level set solver, using a twice finer mesh in each spatial direction for the level set solver as compared to the flow solver.

As discussed in more detail in appendix A, solution verification for RMI in the inviscid limit requires either decoupling of the mesh spacing from the resolved wavelength, by explicit filtering with a constant filter size, or the introduction of regularization to suppress the growth of higher wavenumbers initiated by numerical errors. Here we will follow the latter approach, since regularization by physical properties like viscosity or surface tension not only allows us to demonstrate convergence of the numerical simulation to the theoretical prediction, but also enables the study of how small values of viscosity and surface tension found in applications can influence flow behaviour compared to the idealized conditions of the theory.

The following sections report simulation results for three different Atwood numbers, $A = 0.4$, $A = 0.55$ and $A = 0.9$, for different initial disturbance amplitudes ε, for viscosity, always set equal in the two fluids, i.e. $\mu_1 = \mu_2 = \mu$, and/or for surface tension, using flow solver grid resolutions of $\lambda/\Delta x = 512$ (grid $g512$), and $\lambda/\Delta x = 1024$ (grid $g1024$), with a twice finer level set mesh. Details of the actual simulation parameters used are provided in the respective sections, together with the employed flow solver mesh resolution in the captions of the respective figures.

4. Simulation results

4.1. *Weakly nonlinear and intermediate time evolution*

Figure 10 exhibits spike curvature evolution for three values of dimensionless viscosity: $\mu = 1.0 \times 10^{-4}$, 0.4×10^{-4} and 0.2×10^{-4}. While viscosity appears to have only a minor impact on the initial evolution of the spike curvature ($kAUt < 9$), the maximum curvature of the spike increases with increasing viscosity. This difference persists and is amplified for intermediate times resulting in more curved spike geometries for increasing viscosity at a given intermediate time. Comparing the numerical results for reduction of viscosity towards the inviscid limit of the theory, we see excellent convergence of the simulation to the theoretical results.

Figure 11 shows the bubble curvature evolution for viscosities of $\mu = 10^{-4}$ and $\mu = 0.4 \times 10^{-4}$ compared to the nonlinear theoretical analysis. Both simulation results show virtually identical behaviour for larger times, within the range of solutions predicted by the theory. At early times, both simulation results track the theoretical predictions well, while at intermediate times between 5 and 20 the lower viscosity simulation seems to follow the theoretical prediction marginally better. Overall, viscosity seems to have a significantly smaller impact on bubble curvature than on spike curvature. Virtually no difference can be discerned between the two viscosity cases for $kAUt > 25$. The simulated normalized curvature appears to saturate at $1/(kR_b) \approx 0.4$, a larger value than $1/3$ predicted by all versions of the Layzer model for RMI; cf. Mikaelian (1998), Zhang (1998) and Goncharov (2002). The theory developed by Abarzhi (2002),

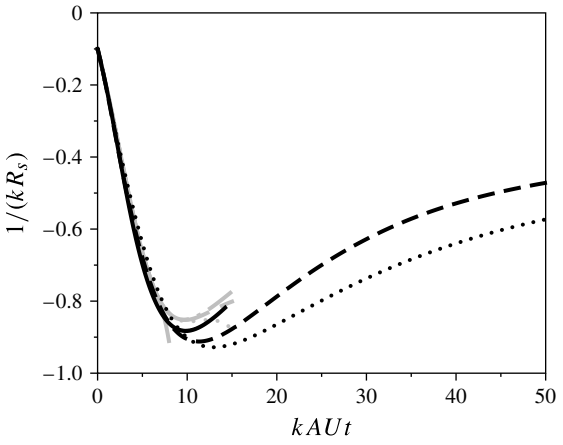

FIGURE 10. The impact of viscosity on the evolution of the spike curvature for Atwood number $A = 0.55$, initial amplitude $\varepsilon = 0.1$, $\lambda/\Delta x = 512$, $\mu = 10^{-4}$ (dotted black line), $\mu = 0.4 \times 10^{-4}$ (dashed black line), and $\mu = 0.2 \times 10^{-4}$ (solid black line), in comparison with weakly nonlinear theoretical analysis (grey lines).

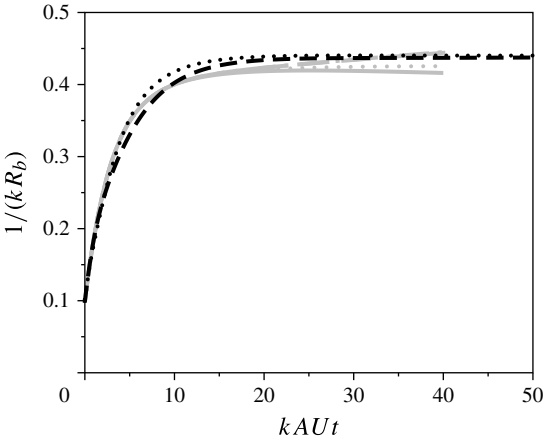

FIGURE 11. The impact of viscosity on the evolution of the bubble curvature for Atwood number $A = 0.55$, initial amplitude $\varepsilon = 0.1$, $\lambda/\Delta x = 512$, $\mu = 10^{-4}$ (dotted black line), $\mu = 0.4 \times 10^{-4}$ (dashed black line), in comparison with weakly nonlinear theoretical analysis (grey lines).

Abarzhi *et al.* (2003) and Abarzhi (2008) for RMI in the late-time, strongly nonlinear limit of $t \to \infty$, $k\eta \to \infty$, predicts asymptotic flattening of the bubble tip, $1/(kR_b) \to 0$, which has been confirmed in numerical simulations by Herrmann *et al.* (2008). This asymptotic regime has not been reached here.

Figure 12 shows the average perturbation amplitude $k\eta = \frac{1}{2}k(\eta_b - \eta_s)$ for the same conditions as in figures 10 and 11. Here and below, some of the grey curves representing successive Padé approximants might not be visible in the figures if the lines are superimposed due to convergence. Increasing viscosity results in a reduction in the amplitude at a given instance in time but, on reducing viscosity, we see good

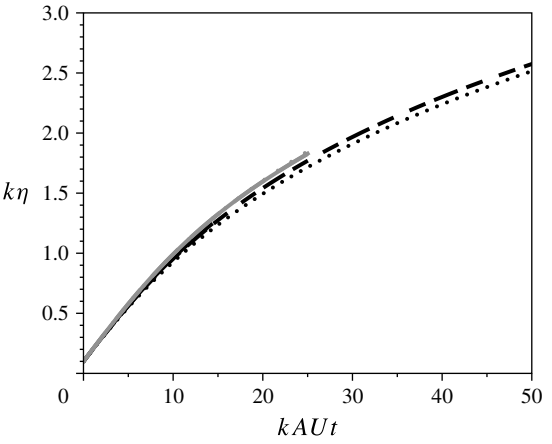

FIGURE 12. The impact of viscosity on the evolution of average amplitude for Atwood number $A = 0.55$, initial amplitude $\varepsilon = 0.1$, $\lambda/\Delta x = 512$, $\mu = 10^{-4}$ (dotted black line), $\mu = 0.4 \times 10^{-4}$ (dashed black line), and $\mu = 0.2 \times 10^{-4}$ (solid black line), compared to nonlinear theory predictions: Padé approximants P_6^6 (solid grey line), P_8^8 (dashed grey line), and P_{10}^{10} (dotted grey line).

agreement between simulation and theory over the whole range of convergence, up to $k\eta \sim 1.5$.

4.2. *Spike acceleration*

To study the difference in acceleration behaviour predicted by the nonlinear theory for different Atwood numbers and initial disturbance amplitudes, three different cases were simulated; see figure 5. Case (*a*) is identical to the Atwood number $A = 0.55$, initial amplitude $\varepsilon = 0.1$ discussed in the previous section, whereas case (*b*) uses an Atwood number of $A = 0.9$ with initial amplitude $\varepsilon = 0.1$. For both cases, the nonlinear theory predicts spike acceleration. Case (*c*) uses an Atwood number of $A = 0.4$ with initial amplitude $\varepsilon = 0.5$. For this case, the nonlinear theory predicts no acceleration of the spike, whereas the approximate formula (36) of Dimonte & Ramaprabhu (2010) does predict initial spike acceleration.

Figure 13 shows a comparison of the simulation results for case (*a*), for ever smaller viscosities, compared to the nonlinear theory. All simulations show an initial acceleration of the spike, followed by a deceleration. Increasing viscosity results in a reduction of the initial acceleration. Thus it is conceivable that adding sufficient viscosity might be used to suppress the initial acceleration.

Reducing the viscosity from 0.4×10^{-4} to 0.05×10^{-4} clearly results in simulation results that approach the theoretically predicted spike velocity behaviour. It was found, however, that at the chosen flow solver mesh resolution of $\lambda/\Delta x = 1024$, in order to suppress the growth of higher wavenumber disturbances at viscosities of $\mu = 0.1 \times 10^{-4}$ and below, the addition of a small amount of surface tension, $\sigma = 10^{-6}$ to regularize the solution further is necessary.

The symbols in figure 13 mark the time and spike velocity at the start of spike deceleration. Increasing viscosity results in an earlier start of deceleration. Reducing viscosity systematically to approach the inviscid limit of the theory, the simulation results clearly approach the time and spike velocity value $kAUt_s = 4.5$ given by (2.41)

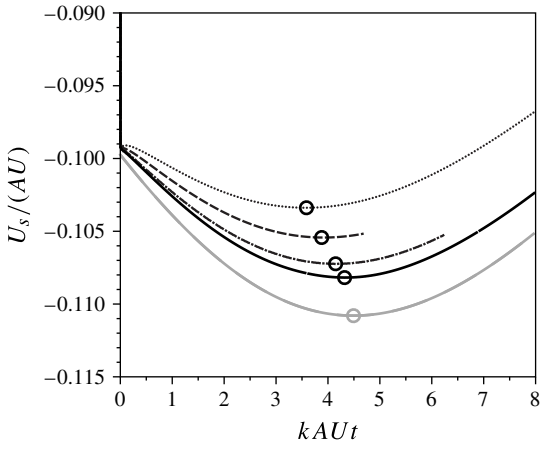

FIGURE 13. The impact of viscosity and surface tension on spike velocity vs. time for $A = 0.55$, $\varepsilon = 0.1$, $\lambda/\Delta x = 1024$ and $\mu = 0.4 \times 10^{-4}$ (black dotted line), $\mu = 0.2 \times 10^{-4}$ (black dashed line), $\mu = 0.1 \times 10^{-4}$ and $\sigma = 10^{-6}$ (black dash/dotted line), $\mu = 0.05 \times 10^{-4}$ and $\sigma = 10^{-6}$ (black solid line), compared to nonlinear theory predictions: Padé approximants P_6^6 (grey solid line) and P_8^8 (grey dashed line). The symbols mark the start of spike deceleration.

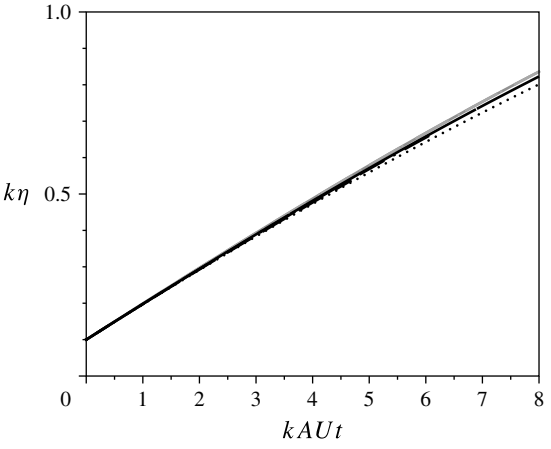

FIGURE 14. The impact of viscosity and surface tension on the evolution of average amplitude for $A = 0.55$, $\varepsilon = 0.1$, $\lambda/\Delta x = 1024$, $\mu = 0.4 \times 10^{-4}$ (black dotted line), $\mu = 0.2 \times 10^{-4}$ (black dashed line), $\mu = 0.1 \times 10^{-4}$ and $\sigma = 10^{-6}$ (black dash/dotted line), $\mu = 0.05 \times 10^{-4}$ and $\sigma = 10^{-6}$ (black solid line), compared to nonlinear theory predictions: Padé approximants P_6^6 (grey solid line), P_8^8 (grey dashed line), and P_{10}^{10} (grey dotted line).

(which for a small $\varepsilon = 0.1$ is a good approximation of the exact prediction of the nonlinear theory). The residual discrepancy between the predicted peak velocity of the spike and its numerical estimate is due to the difference between the theoretical and numerical velocity profiles. The former exhibits a sharp peak at the tip of the spike shown in figure 8, whereas in the latter the velocity peak is inevitably smoothed; see § 4.3 for details.

Figure 14 shows the time history of the average perturbation amplitude $k\eta$, as in figure 12, for the conditions and time range of figure 13 (this is, of course, a zoomed

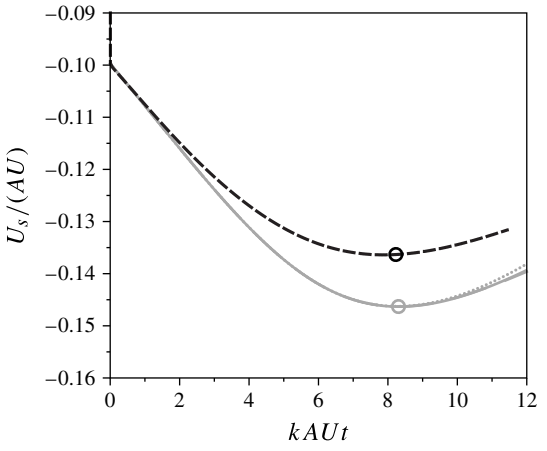

FIGURE 15. Spike velocity vs. time for $A = 0.9$, $\varepsilon = 0.1$, $\lambda/\Delta x = 512$, $\mu = 0.2 \times 10^{-4}$ (black dashed line), compared to nonlinear theory predictions: Padé approximants P_6^6 (grey solid line), P_8^8 (grey dashed line), and P_{10}^{10} (grey dotted line). The symbols mark the start of spike deceleration.

fragment of figure 12). In this time range we see excellent agreement between theory and simulation and good convergence of the simulation results to the theory prediction with decreasing viscosity. Only the largest value of viscosity, $\mu = 0.4 \times 10^{-4}$, exhibits any appreciable reduction in the amplitude at later times, indicating that amplitude is relatively insensitive to low viscosity.

Figure 15 shows the spike velocity as a function of time for case (*b*) simulated using a viscosity of $\mu = 0.2 \times 10^{-4}$. The symbols mark the spike velocity and moment in time for the onset of spike deceleration which, according to theory, is slightly later than the value $kAUt_s = 8$ predicted by (2.41). Excellent agreement between the simulation result and the theoretical prediction is achieved. Figure 16 presents the time history of the average amplitude $k\eta$ for the same case. Here again we see good agreement between simulation and theory, although the influence of viscosity on the amplitude appears to be larger in this case than in case (*a*); compare figure 14.

Finally, figure 17 shows the spike velocity as a function of time for case (*c*) simulated using the same viscosity of $\mu = 0.2 \times 10^{-4}$ used in case (*b*). As predicted by the present nonlinear theory, and contrary to the prediction of the approximate formula of Dimonte & Ramaprabhu (2010), the simulation results show no evidence for acceleration of the spike. Figure 18 shows the time history of the average amplitude $k\eta$ for the same case. The agreement between simulation and theory is still good, even though the coefficients of the Taylor series (2.24) are known here with much lower accuracy compared to figures 10–16; see § 2.3.

4.3. *Velocity field*

Figure 19 compares the simulated vertical velocity profiles at bubble location $x = 0$ with the theoretical profiles for the conditions of figure 7(*b*) at $kAUt = 2$, 4, 6 and 8. The theoretical profiles from figure 7(*b*) are shown here as solid grey lines. Simulation results are presented for the smallest value of viscosity $\mu = 0.05 \times 10^{-4}$. We see very good agreement everywhere except in the vicinity of the bubble tip, where the discontinuity in $\partial u_y/\partial y$ predicted by theory is smoothed by dissipation caused by the

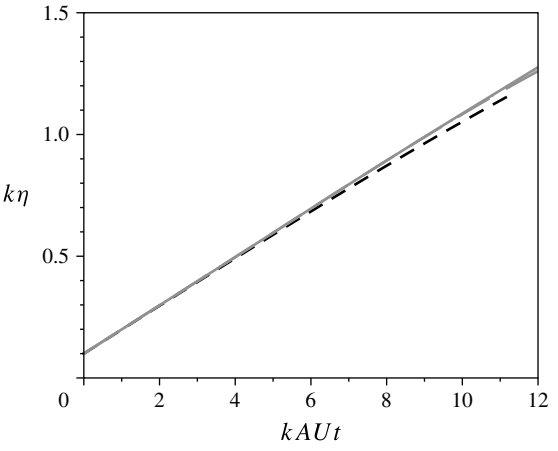

FIGURE 16. The evolution of average amplitude for $A = 0.9$, $\varepsilon = 0.1$, $\lambda/\Delta x = 512$, $\mu = 0.2 \times 10^{-4}$ (black dashed line), compared to nonlinear theory predictions: Padé approximants P_6^6 (grey solid line), P_8^8 (grey dashed line), and P_{10}^{10} (grey dotted line).

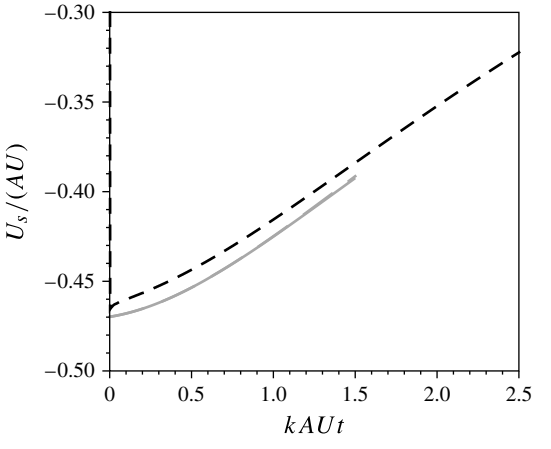

FIGURE 17. Spike velocity vs. time for $A = 0.4$, $\varepsilon = 0.5$, $\lambda/\Delta x = 512$, $\mu = 0.2 \times 10^{-4}$ (black dashed line), compared to nonlinear theory predictions: Padé approximants P_6^6 (grey solid line), P_8^8 (grey dashed line), and P_{10}^{10} (grey dotted line). No acceleration of the spike has been predicted or can be observed.

introduction of viscosity. The simulation is seen to capture the early-time growth of velocity of the heavy fluid for a given y in the vicinity of the initial bubble position $y = \eta_b$ discussed in § 2.6.

Figure 20 demonstrates the impact of viscosity on the velocity profile plotted in figure 19 for $kAUt = 8$. For larger values of the viscosity, the peak in vertical velocity is more pronounced and shifts further into the light fluid, resulting in a noticeable different vertical velocity in the lower fluid close to the interface. This difference decays with increasing distance from the interface and is almost entirely gone at a distance of roughly $ky = 3$ from the interface. The simulated profiles however do converge to the theoretical prediction of figure 6(*b*) as the viscosity is reduced from $\mu = 0.2 \times 10^{-4}$ to $\mu = 0.05 \times 10^{-4}$. Strikingly, the vertical velocity in the heavy fluid

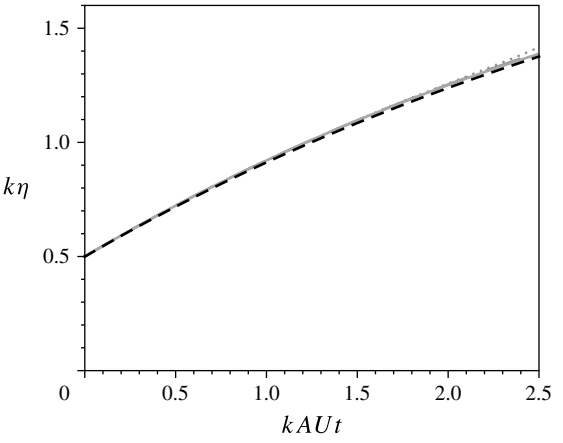

FIGURE 18. The evolution of average amplitude for $A = 0.4$, $\varepsilon = 0.5$, $\lambda/\Delta x = 512$, $\mu = 0.2 \times 10^{-4}$ (black dashed line), compared to nonlinear theory predictions: Padé approximants P_6^6 (grey solid line), P_8^8 (grey dashed line), and P_{10}^{10} (grey dotted line).

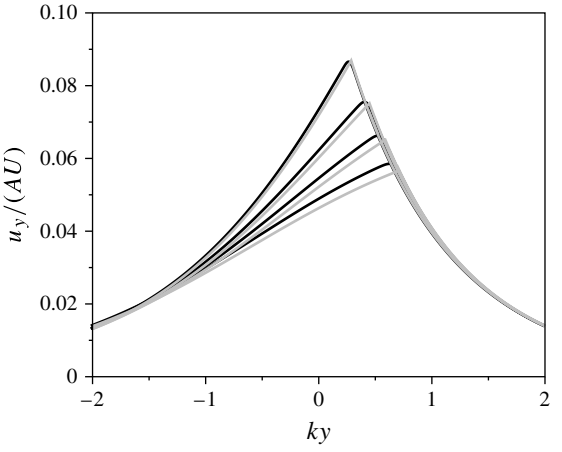

FIGURE 19. Vertical velocity at bubble position at $kAUt = 2$, 4, 6 and 8 (from left to right) for $A = 0.55$, $\varepsilon = 0.1$, $\lambda/\Delta x = 1024$, $\mu = 0.05 \times 10^{-4}$, $\sigma = 10^{-6}$ (black solid lines), compared to nonlinear theory predictions (grey solid lines).

is significantly less sensitive to variations in viscosity, to the effect that the velocity there agrees with the inviscid prediction of the theory for all analysed values of the viscosity.

Figure 21 shows the vertical velocity profiles obtained for the same conditions as in figure 7(*b*) at $kAUt = 5$, 10, 15, 20 and 25, for the smallest value of the viscosity $\mu = 0.05 \times 10^{-4}$, i.e. the case that most closely resembles theory. There are no theoretical results to compare with the profiles plotted for $kAUt = 10$ and later times. Still, it is interesting to check if the trends noticed at early times in § 2.6 still hold. Indeed, we see that the velocity of the heavy fluid keeps decreasing for a given y, the trend noticeable in figure 7(*b*), and still peaks at the bubble tip. For a given y close to the bubble tip, the velocity of the light fluid decreases with time, as in figure 7(*b*), whereas far from the tip it increases. As a result of this evolution the peak of the

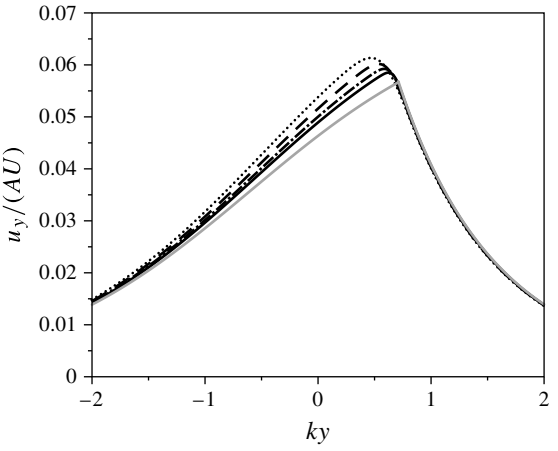

FIGURE 20. The impact of viscosity and surface tension on the vertical velocity at the bubble position at $kAUt = 8$ for $A = 0.55$, $\varepsilon = 0.1$, $\lambda/\Delta x = 1024$, $\mu = 0.4 \times 10^{-4}$ (black dotted line), $\mu = 0.2 \times 10^{-4}$ (black dashed line), $\mu = 0.1 \times 10^{-4}$ and $\sigma = 10^{-6}$ (black dash/dotted line), $\mu = 0.05 \times 10^{-4}$ and $\sigma = 10^{-6}$ (black solid line), compared to nonlinear theory prediction (grey solid line).

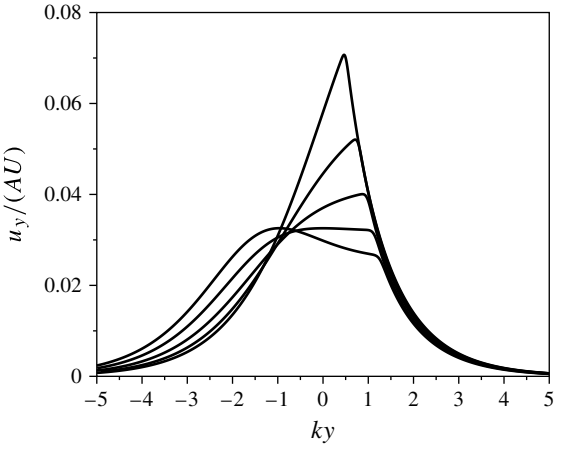

FIGURE 21. Vertical velocity at bubble position at $kAUt = 5$, 10, 15, 20 and 25 (from top to bottom) for $A = 0.55$, $\varepsilon = 0.1$, $\lambda/\Delta x = 1024$, $\mu = 0.05 \times 10^{-4}$ and $\sigma = 10^{-6}$.

light fluid velocity shifts from the tip of the bubble, as in figure 7(*b*), into the bulk of the light fluid. At $kAUt = 20$ the peak is flat and still adjacent to the tip, whereas at a later time, at $kAUt = 25$, the peak becomes sharper and definitely distinct from the tip. The derivative $\partial u_y/\partial y$ in the light fluid changes sign and becomes negative in the vicinity of the bubble tip.

Figure 22 demonstrates the impact of viscosity on the velocity profile plotted in figure 21 for $kAUt = 25$. As was observed at $kAUt = 8$ in figure 20, even at this later stage, viscosity has a negligible impact on the heavy fluid vertical velocity and only a small impact on the vertical velocity in the light fluid when moving sufficiently far away from the interface. However, for smaller distances to the interface in the

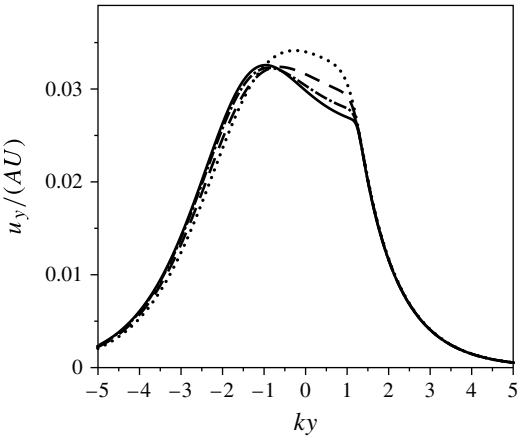

FIGURE 22. The impact of viscosity and surface tension on the vertical velocity at bubble position at $kAUt = 25$ for $A = 0.55$, $\varepsilon = 0.1$, $\lambda/\Delta x = 1024$, $\mu = 0.4 \times 10^{-4}$ (black dotted line), $\mu = 0.2 \times 10^{-4}$ (black dashed line), $\mu = 0.1 \times 10^{-4}$ and $\sigma = 10^{-6}$ (black dash/dotted line), $\mu = 0.05 \times 10^{-4}$ and $\sigma = 10^{-6}$ (black solid line).

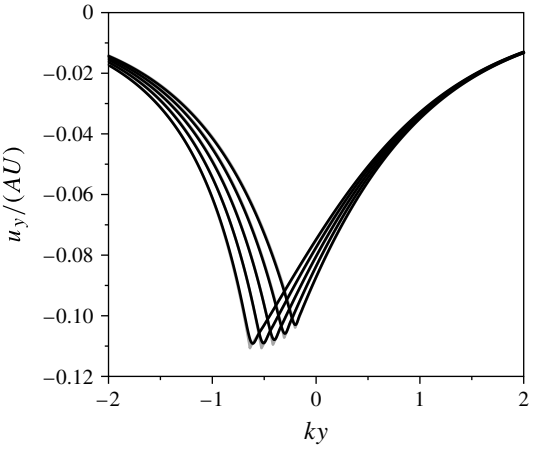

FIGURE 23. Vertical velocity at spike position at $kAUt = 1$, 2, 3, 4 and 5 (from right to left) for $A = 0.55$, $\varepsilon = 0.1$, $\lambda/\Delta x = 1024$, $\mu = 0.05 \times 10^{-4}$, $\sigma = 10^{-6}$ (black solid lines), compared to nonlinear theory predictions (grey solid lines).

light fluid, viscosity has a significant impact. The generation of a distinct second peak in vertical velocity away from the interface can be suppressed with sufficiently large viscosities. However figure 22 demonstrates how the velocity profiles converge to the profile shown in figure 23 as the viscosity is reduced from $\mu = 0.2 \times 10^{-4}$ to 0.05×10^{-4} to approach the inviscid limit.

Figure 23 compares the simulated vertical velocity profiles at spike location $kx = \pi$ with the theoretical profiles for the conditions of figure 8(*b*) at $kAUt = 1$, 2, 3, 4, and 5. Once again, the theoretical profiles from figure 8(*b*) are shown as solid grey lines, and simulation results are presented for the smallest value of the viscosity $\mu = 0.05 \times 10^{-4}$. Compared to the bubble location, the spike location velocity profiles appear to be significantly less sensitive to small amounts of viscosity (see figure 24).

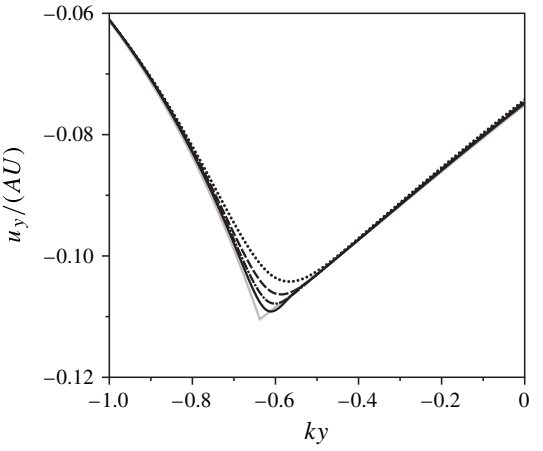

FIGURE 24. The impact of viscosity and surface tension on the vertical velocity at spike position at $kAUt = 5$ for $A = 0.55$, $\varepsilon = 0.1$, $\lambda/\Delta x = 1024$, $\mu = 0.4 \times 10^{-4}$ (black dotted line), $\mu = 0.2 \times 10^{-4}$ (black dashed line), $\mu = 0.1 \times 10^{-4}$ and $\sigma = 10^{-6}$ (black dash/dotted line), $\mu = 0.05 \times 10^{-4}$ and $\sigma = 10^{-6}$ (black solid line), compared to nonlinear theory prediction (grey solid line).

In fact agreement with the inviscid theory is excellent, except for the vicinity of the spike tip, where the sharp velocity peaks of figure 8(*b*) are smoothed by dissipation due to viscosity. This effect is more clearly shown in figure 26, showing the velocity profile for $kAUt = 5$ and increasing values of viscosity. Only in the direct vicinity of the interface is the sharp peak of the inviscid solution smoothed by viscous forces, but only a short distance away this effect becomes negligible for the vertical velocity. Analysing the limit of vanishing viscosity to approach the inviscid limit of the theory, the simulation results appear to converge well to the theoretical prediction of figure 8(*b*).

Figure 25 shows the profiles of vertical velocity for spike location $kx = \pi$ at $kAUt = 5$, 10, 15, 20 and 25. There are no theoretical results to compare with the profiles plotted for $kAUt = 10$ and later times. Still, the trends discussed in § 2.6 are seen to hold. For a given y, the velocity of the light fluid is seen to increase until the tip of the spike passes this location and the velocity of the heavy fluid starts to decrease, as in figure 8. As a result, the velocity of the light fluid always peaks at the tip of the spike. The peak of the heavy fluid velocity coincides with the tip of the spike at early time and then shifts into the bulk of the heavy fluid after $kAUt = 10$. The derivative $\partial u_y/\partial y$ in the heavy fluid changes sign and becomes negative in the vicinity of the spike tip. Comparing figures 21 and 25, we can conclude that the velocity profiles of the light and heavy fluids evolve in a qualitatively similar way at bubble and spike positions, respectively.

Figure 26 analyses the impact of viscosity on the spike position vertical velocity profiles. While the peak of the heavy fluid velocity decreases slightly with increasing viscosity, the changes caused by viscosity are only minor compared to the influence of viscosity on the bubble position vertical velocity profile; compare figure 22.

Figure 27 compares the simulated profiles of horizontal velocity halfway between bubble and spike positions, at $kx = \pi/2$, with the theoretical profiles for the conditions of figure 9(*b*) at $kAUt = 2$, 4, 6, and 8 (from top to bottom at $y > 0$). The theoretical

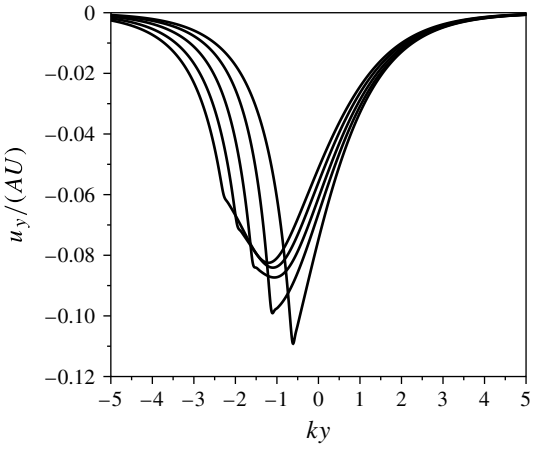

FIGURE 25. Vertical velocity at spike position at $kAUt = 5$, 10, 15, 20 and 25 (from top to bottom) for $A = 0.55$, $\varepsilon = 0.1$, $\lambda/\Delta x = 1024$, $\mu = 0.05 \times 10^{-4}$ and $\sigma = 10^{-6}$.

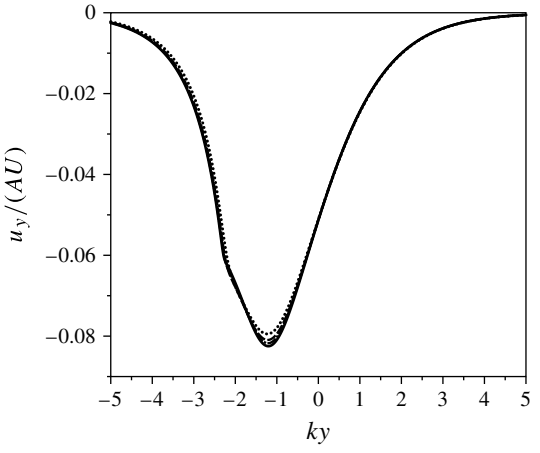

FIGURE 26. The impact of viscosity and surface tension on the vertical velocity at spike position at $kAUt = 25$ for $A = 0.55$, $\varepsilon = 0.1$, $\lambda/\Delta x = 1024$, $\mu = 0.4 \times 10^{-4}$ (black dotted line), $\mu = 0.2 \times 10^{-4}$ (black dashed line), $\mu = 0.1 \times 10^{-4}$ and $\sigma = 10^{-6}$ (black dash/dotted line), $\mu = 0.05 \times 10^{-4}$ and $\sigma = 10^{-6}$ (black solid line).

profiles from figure 9(*b*) are shown here as solid grey lines, and simulation results are presented for the smallest value of the viscosity $\mu = 0.05 \times 10^{-4}$. Note that at the material interface, the theoretical solution is itself discontinuous, not just its derivative, as in figures 19 and 23. Agreement between simulation and theory is excellent everywhere, except in the immediate vicinity of the interface, where the discontinuities present both in the horizontal velocity and in its vertical derivative have been smoothed due to viscosity. The impact of viscosity on the horizontal velocity profile is further demonstrated in figure 28 for $kAUt = 8$. The simulated profiles are seen to converge to the one shown in figure 27 and are very close to the theoretical prediction of figure 9(*b*) as the viscosity is reduced from $\mu = 0.2 \times 10^{-4}$ to 0.05×10^{-4}. Viscosity appears to have a negligible impact on the heavy fluid

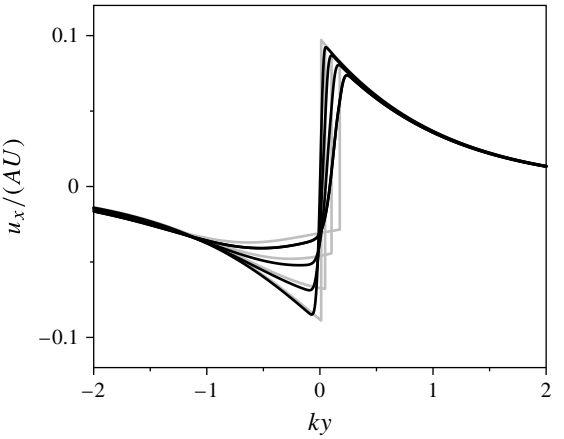

FIGURE 27. Horizontal velocity halfway between bubble and spike positions, at $kx = \pi/2$, at $kAUt = 2$, 4, 6, and 8 (from top to bottom at $y > 0$) for $A = 0.55$, $\varepsilon = 0.1$, $\lambda/\Delta x = 1024$, $\mu = 0.05 \times 10^{-4}$, $\sigma = 10^{-6}$ (black solid lines), compared to nonlinear theory predictions (grey solid lines).

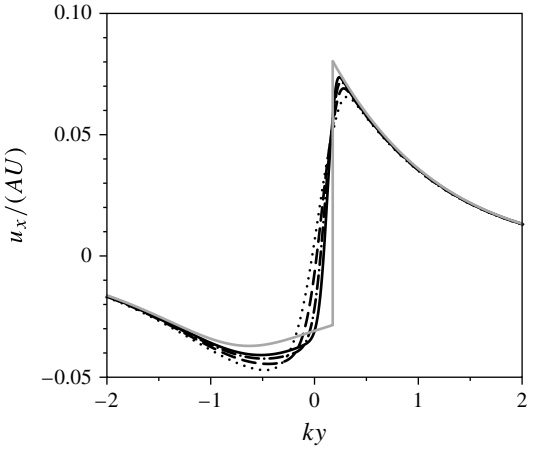

FIGURE 28. The impact of viscosity and surface tension on the horizontal velocity halfway between bubble and spike positions, at $kx = \pi/2$, at $kAUt = 8$ for $A = 0.55$, $\varepsilon = 0.1$, $\lambda/\Delta x = 1024$, $\mu = 0.4 \times 10^{-4}$ (black dotted line), $\mu = 0.2 \times 10^{-4}$ (black dashed line), $\mu = 0.1 \times 10^{-4}$ and $\sigma = 10^{-6}$ (black dash/dotted line), $\mu = 0.05 \times 10^{-4}$ and $\sigma = 10^{-6}$ (black solid line), compared to nonlinear theory prediction (grey solid line).

horizontal velocity, except right at the interface, where the discontinuity in velocity is smoothed by viscous forces. However, the horizontal velocity in the light fluid is strongly impacted by viscosity, generating a pronounced maximum away from the interface with increasing viscosity. However, as observed before, some distance away from the interface the changes induced by viscous forces are negligible and the viscous solutions approach the inviscid theoretical predictions.

Finally, figure 29 shows the profiles of horizontal velocity at the same location for later time $kAUt = 5$, 10, 15, 20 and 25. A peak of horizontal velocity of the light fluid is observed to develop by $kAUt = 25$ at about the same vertical position $ky = -1$

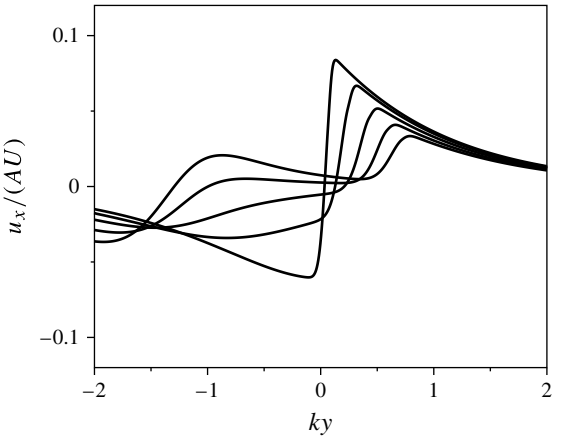

FIGURE 29. Horizontal velocity halfway between bubble and spike positions, at $kx = \pi/2$, at $kAUt = 5$, 10, 15, 20 and 25 (from top to bottom at $y > 0$) for $A = 0.55$, $\varepsilon = 0.1$, $\lambda/\Delta x = 1024$, $\mu = 0.05 \times 10^{-4}$ and $\sigma = 10^{-6}$.

where the peaks of vertical velocity of the light fluid at the bubble position (figure 21) and of the heavy fluid at the spike position (figure 23) are seen.

5. Conclusion

We conducted a study of 2D incompressible RMI at weakly and moderately nonlinear stages of its evolution by doing numerical simulations and systematically comparing them to the theoretical analysis. Our theory, based on high-order perturbation expansion, has been demonstrated to converge, providing accurate predictions for amplitudes, velocities and curvatures of bubbles and spikes, up to the moderately nonlinear stage of the RMI development, when the average amplitude $k\eta \sim 1$–1.5. In particular, the theory accurately delineates the parameter ranges in the plane (ε, A) that correspond to the presence or absence of early-time acceleration of the spike and the bubble, which cannot be done with heuristic phenomenological models. For the situation when the spike or the bubble initially accelerates, we derived an accurate approximate formula (2.41) predicting the instant of time when the acceleration stops and the deceleration begins.

We have confirmed the predictions made by the theory using numerical simulations. Although we found that simulations require the introduction of regularization in the form of viscosity, by systematically reducing viscosity one can recover the theoretically predicted results of the inviscid limit. Our analysis thus provides reliable quantitative verification benchmarks for the early and intermediate time evolution of RMI.

The current theory assumes inviscid fluids, as in fact do most of the theories of RMI evolution. In applications for real fluids, this is an idealization and we thus studied the impact of non-zero viscosity on the evolution of RMI using numerical simulations. We found that amplitude, initial spike acceleration or deceleration, bubble curvature, heavy fluid spike and bubble position vertical velocity profiles, light fluid spike position vertical velocity profiles, and heavy fluid midpoint horizontal velocity profiles are only weakly impacted by viscosity, so our theory will give predictions for these quantities that are directly applicable to most real world applications. However, spike curvature,

maximum spike velocity, near interface light fluid bubble position vertical velocity profiles, and light fluid midpoint horizontal velocity profiles do depend on viscosity of the fluids and therefore the theoretical predictions of our model have to be considered carefully in real world applications of viscous fluids.

An important result of our study is the velocity flow field. Our analysis provides reliable quantitative verification benchmarks for the early and intermediate time evolution of RMI. In the past it was argued that, on the one hand, rigorous benchmarks are impossible to develop for RMI, since the weakly nonlinear analysis diverges for any time and at any value of the initial amplitude. On the other hand, it was presumed that the basic physics of RMI can be fully described by phenomenological models with adjustable parameters. Even the most elaborate such models sometimes yield wrong predictions, as in our example of early-time spike acceleration.

It is clear from the mathematical analysis (Wu 1999), weakly nonlinear theories (Velikovich & Dimonte 1996; Berning & Rubenchik 1998; Holmes *et al.* 1999) and our present results that, while the circle of convergence of the weakly nonlinear expansion series in the complex time plane is indeed finite, the series generate analytic functions of complex time and perturbation amplitude (2.7), which in many cases can be analytically continued beyond their respective circles of convergence with the use of Padé approximation or other techniques. For these cases the theory successfully describes weakly nonlinear development for a finite time after the instability starts to grow. The flow complexity at the later time is reflected in the increasingly complex geometry of the Riemann surfaces defined by those functions far from the origin $t = 0$. At this stage simple tools of analytic continuation no longer work, and the theory lacks the mathematical technique necessary to extend the exact analysis to later times. The characteristic time scale for divergence of the series is most likely associated with the process of 'mushrooming' of the spike, after which the Eulerian single-valued description of the perturbed interface as $y = \eta(x, t)$ is no longer possible.

Although the detailed study of highly nonlinear incompressible RMI is beyond the scope of the present paper, our theoretical and numerical results clearly indicate that a reliable description of RMI requires a solution of a boundary value problem. Our numerical simulations clearly demonstrate that careful control of regularization and grid refinement are key to finding accurate numerical solutions, achieving convergence of these solutions, and obtaining excellent quantitative agreement with the perturbation theory.

Acknowledgements

A.L.V. is grateful to G. Dimonte and G. Hazak for many stimulating discussions. This work was supported by US DOE/NNSA (A.L.V.), and US NSF (S.I.A).

Appendix. Solution verification

Figure 30 shows a mesh refinement study of the evolution of the velocity and curvature of the spike and bubble and its comparison with the weakly nonlinear theory for the case of $A = 0.55$ and initial amplitude $\varepsilon = 0.1$. Four different flow solver mesh resolutions, $\lambda/\Delta x = 32$, 64, 128, and 256, each run with a twice finer level set mesh, are compared to theoretical predictions. Since the theoretical analysis is conducted in the inviscid limit, the simulations are performed with zero viscosity and zero surface tension. While the numerical results of the velocity and, especially, the bubble velocity seem to suggest that grid convergence to theoretically

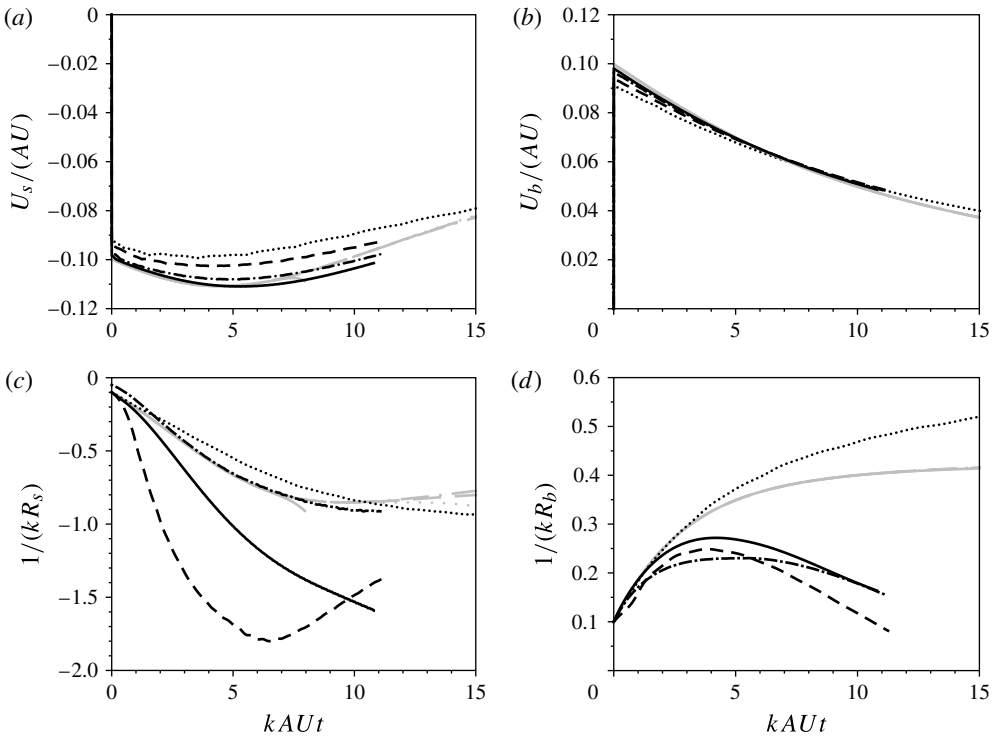

FIGURE 30. Grid refinement study for inviscid, immiscible fluids at $\lambda/\Delta x = 32$ (dotted black line), $\lambda/\Delta x = 64$ (dashed black line), $\lambda/\Delta x = 128$ (dot-dashed black line) and $\lambda/\Delta x = 256$ (solid black line) in comparison to the weakly nonlinear theoretical analysis (grey lines) for Atwood number $A = 0.55$ and initial amplitude $\varepsilon = 0.1$. (*a*) Spike velocity; (*b*) bubble velocity; (*c*) spike curvature; (*d*) bubble curvature.

predicted velocities is possible, the results for the curvature clearly indicate that no grid convergence for the solution is obtained. The reason is that the simulations are performed without any viscosity and surface tension for two immiscible fluids, thus no regularization is introduced other than dissipative errors of the employed numerical schemes. Since refining the mesh resolves higher and higher wavenumbers in the simulation, and since, according to the theory, these waves have faster and faster growth rates, any numerical error, induced either by finite precision round-off or the truncation errors of finite-order numerical methods, provides sufficient initial amplitudes for those higher wave numbers to result in large enough later time amplitudes to pollute the solution. This is clearly evident in figure 31, which shows the immiscible interface shape for a flow solver mesh with $\lambda/\Delta x = 256$ and a twice finer level set mesh. While the theoretical analysis does include the growth of higher wavenumbers, their amplitude is initially set to zero in the theory and thus only emerge gradually, as a result of nonlinear interaction between lower-order modes.

The conundrum that mesh refinement is required for solution verification in order to reduce numerical error, while at the same time enables the ever-faster growth of the smallest resolved wavelengths, can likely be addressed only in two ways: either by explicitly filtering the interface, thereby decoupling the mesh spacing from the resolved wavelength, or by introducing a physical regularization by viscosity or surface tension. Here, we will follow the latter approach. Thus the limit of these

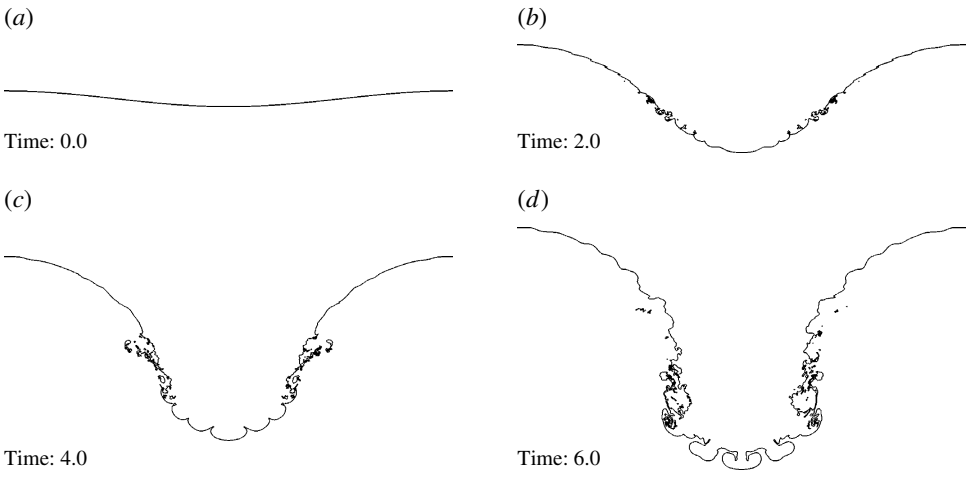

FIGURE 31. The evolution of the interface separating inviscid, immiscible fluids with no surface tension and Atwood number $A = 0.55$, initial amplitude $\varepsilon = 0.1$, flow solver mesh resolution $\lambda/\Delta x = 256$, for a single mode initial perturbation at dimensionless time (*a*) $kAUt = 0$, (*b*) 6.9, (*c*) 13.8 and (*d*) 20.7.

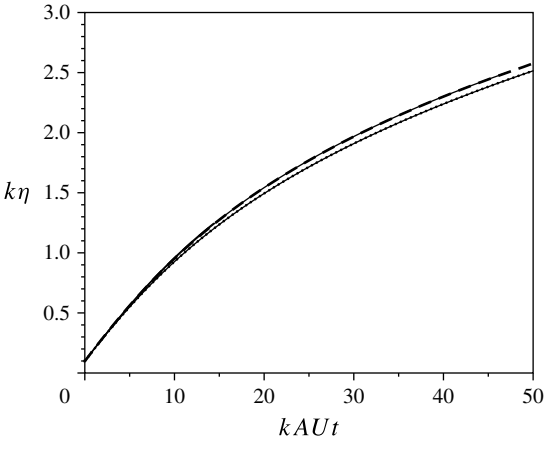

FIGURE 32. The evolution of average amplitude for Atwood number $A = 0.55$, initial amplitude $\varepsilon = 0.1$, flow solver mesh resolution $\lambda/\Delta x = 256$ (thin black lines) and $\lambda/\Delta x = 512$ (thick black lines), with $\mu = 10^{-4}$ (dotted black lines) and $\mu = 0.4 \times 10^{-4}$ (dashed black lines).

regularizations going to zero has to be studied, in addition to the necessary solution verification by mesh refinement. The resulting decoupling of physical regularization (viscosity, surface tension) from numerical regularization (dissipative errors) is key to obtaining verifiable results.

Figure 32 shows the evolution of the average amplitude for two different values of the dimensionless viscosity $\mu = 1.0 \times 10^{-4}$, 0.4×10^{-4} and two different flow solver grid resolutions $\lambda/\Delta x = 256$ and 512, each with a twice finer level set mesh. As shown, the two grid resolutions are indistinguishable indicating good grid convergence even for the coarser mesh of $\lambda/\Delta x = 256$. However, amplitude is not as sensitive

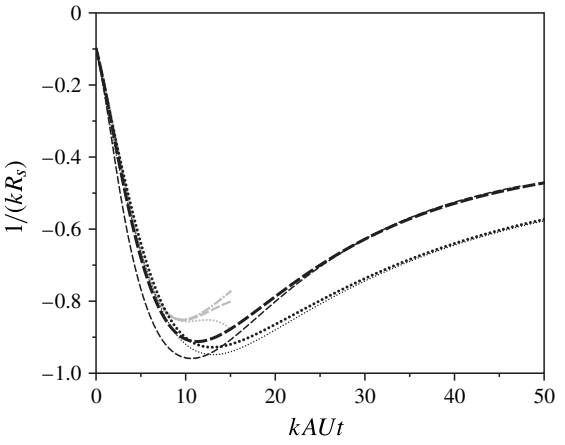

FIGURE 33. The evolution of the spike curvature for Atwood number $A = 0.55$, initial amplitude $\varepsilon = 0.1$, flow solver mesh resolution $\lambda/\Delta x = 256$ (thin black lines) and $\lambda/\Delta x = 512$ (thick black lines), with $\mu = 10^{-4}$ (dotted black lines) and $\mu = 0.4 \times 10^{-4}$ (dashed black lines), in comparison with weakly nonlinear theoretical analysis (grey lines).

an indicator for grid independence as spike curvature, as figure 33 demonstrates. Reducing the viscosity requires increasingly finer meshes to obtain grid-independent results. For instance, for a viscosity of $\mu = 1.0 \times 10^{-4}$, a grid resolution of 256 and 512 mesh points per initial wavelength provide results in excellent agreement with each other, whereas the agreement at $\mu = 0.4 \times 10^{-4}$, while still good, is not of the same high quality. It is interesting to note that grid dependency is prominent only in the vicinity of maximum spike curvature and, for longer times, agreement between different mesh resolutions becomes excellent again, even for $\mu = 0.4 \times 10^{-4}$, explaining why the amplitude results showed good grid convergence throughout.

To ensure results are not unduly influenced by finite mesh resolution, the majority of simulation results reported in this paper are obtained using a flow solver mesh spacing of $\lambda/\Delta x = 1024$. However in cases where regularization by viscosity is sufficiently large, using a flow solver mesh of $\lambda/\Delta x = 512$ provided sufficiently accurate results and was therefore employed.

REFERENCES

ABARZHI, S. I. 2002 A new type of the evolution of the bubble front in the Richtmyer–Meshkov instability. *Phys. Lett.* A **294** (2), 95–100.

ABARZHI, S. I. 2008 Review of nonlinear dynamics of the unstable fluid interface: conservation laws and group theory. *Phys. Scr.* **T132**, 014012.

ABARZHI, S. I. 2010 Review of theoretical modelling approaches of Rayleigh–Taylor instabilities and turbulent mixing. *Phil. Trans. R. Soc. Lond.* A **368** (1916), 1809–1828.

ABARZHI, S. I., GAUTHIER, S. & SREENIVASAN, K. R. 2013 Turbulent mixing and beyond: non-equilibrium processes from atomistic to astrophysical scales. *Phil. Trans. R. Soc. Lond.* A **371**, 20130268.

ABARZHI, S. I., NISHIHARA, K. & GLIMM, J. 2003 Rayleigh–Taylor and Richtmyer–Meshkov instabilities for fluids with a finite density ratio. *Phys. Lett.* A **317** (5–6), 470–476.

AGLITSKIY, Y., KARASIK, M., VELIKOVICH, A. L., SERLIN, V., WEAVER, J. L., KESSLER, T. J., NIKITIN, S. P., SCHMITT, A. J., OBENSCHAIN, S. P., METZLER, N. & OH, J. 2012 Observed

transition from Richtmyer–Meshkov jet formation through feedout oscillations to Rayleigh–Taylor instability in a laser target. *Phys. Plasmas* **10** (10), 102707.

AGLITSKIY, Y., VELIKOVICH, A. L., KARASIK, M., METZLER, N., ZALESAK, S. T., SCHMITT, A. J., PHILLIPS, L., GARDNER, J. H., SERLIN, V., WEAVER, J. L. & OBENSCHAIN, S. P. 2010 Basic hydrodynamics of Richtmyer–Meshkov-type growth and oscillations in the inertial confinement fusion-relevant conditions. *Phil. Trans. R. Soc. Lond.* A **368** (1916), 1739–1768.

ALON, U., HECHT, J., MUKAMEL, D. & SHVARTS, D. 1994 Scale invariant mixing rates of hydrodynamically unstable interfaces. *Phys. Rev. Lett.* **72** (18), 2867–2870.

ALON, U., HECHT, J., OFER, D. & SHVARTS, D. 1995 Power-laws and similarity of Rayleigh–Taylor and Richtmyer–Meshkov mixing fronts at all density ratios. *Phys. Rev. Lett.* **74** (4), 534–537.

ANISIMOV, S. I., DRAKE, R. P., GAUTHIER, S., MESHKOV, E. E. & ABARZHI, S. I. 2013 What is certain and what is not so certain in our knowledge of Rayleigh–Taylor mixing? *Phil. Trans. R. Soc. Lond.* A **371**, 20130266.

APRELKOV, O. N., IGONIN, V. V., LEBEDEV, A. I., MYSHKINA, I. YU. & OL'KHOV, O. V. 2010 Numerical and experimental study of Richtmyer–Meshkov instability in condensed matter. *Phys. Scr.* **T142**, 014025.

BAKER, G. A. & GRAVE-MORRIS, P. 1981 *Padé Approximants, Part I: Basic Theory*. Addison-Wesley.

BAKHRAKH, S. M., BEZRUKOVA, I. YU., KOVALEVA, A. D., KOSARIM, S. S. & OL'KHOV, O. V. 2006 Cumulative instability of the surface of condensed substances. *Tech. Phys. Lett.* **32** (2), 103–105.

BENDER, C. M. & ORSZAG, S. A. 1978 *Advanced Mathematical Methods for Scientists and Engineers*. McGraw Hill.

BERNING, M. & RUBENCHIK, A. M. 1998 A weakly nonlinear theory for the dynamical Rayleigh–Taylor instability. *Phys. Fluids* **10** (7), 1564–1587.

BODNER, S. E., COLOMBANT, D. G., GARDNER, J. H., LEHMBERG, R. H., MCCRORY, R. L., SEKA, W., VERDON, C. P., KNAUER, J. P., AFEYAN, B. B. & POWELL, H. T. 1998 Direct-drive laser fusion: status and prospects. *Phys. Plasmas* **5** (5), 1901–1918.

BRACKBILL, J. U., KOTHE, D. B. & ZEMACH, C. 1992 A continuum method for modeling surface tension. *J. Comput. Phys.* **100** (2), 335–354.

BROUILLETTE, M. 2002 The Richtmyer–Meshkov instability. *Annu. Rev. Fluid Mech.* **34**, 445–468.

BUTTLER, W. T., ORÓ, D. M., PRESTON, D. L., MIKAELIAN, K. O., CHERNE, F. J., HIXSON, R. S., MARIAM, F. G., MORRIS, C., STONE, J. B., TERRONES, G. & TUPA, D. 2012 Unstable Richtmyer–Meshkov growth of solid and liquid metals in vacuum. *J. Fluid Mech.* **703**, 60–84.

CARLÈS, P. & POPINET, S. 2001 Viscous nonlinear theory of Richtmyer–Meshkov instability. *Phys. Fluids* **13** (7), 1833–1836.

CHAPMAN, P. R. & JACOBS, J. W. 2006 Experiments on the three-dimensional incompressible Richtmyer–Meshkov instability. *Phys. Fluids* **18** (7), 074101.

COKELET, E. D. 1977 Steep gravity waves in water of arbitrary uniform depth. *Phil. Trans. R. Soc. Lond.* A **286** (1335), 183–230.

COTRELL, D. L. & COOK, A. W. 2007 Scaling the incompressible Richtmyer–Meshkov instability. *Phys. Fluids* **19** (7), 078105.

DESJARDINS, O., BLANQUART, G., BALARAC, G. & PITSCH, H. 2008 High order conservative finite difference scheme for variable density low Mach number turbulent flows. *J. Comput. Phys.* **227** (15), 7125–7159.

DHOTRE, A., RAMAPRABHU, P. & DIMONTE, G. 2008 A detailed numerical investigation of the single-mode Richtmyer–Meshkov instability. *Bull. Am. Phys. Soc.* **53** (15), 157.

DIMONTE, G. 1999 Nonlinear evolution of the Rayleigh–Taylor and Richtmyer–Meshkov instabilities. *Phys. Plasmas* **6** (5), 2009–2015.

DIMONTE, G., MORRISON, J., HULSEY, S., NELSON, D., WEAVER, S., SUSOEFF, A., RON HAWKE, R., SCHNEIDER, M., BATTEAUX, J., DEAN LEE, D. & TICEHURST, J. 1996 A linear electric motor to study turbulent hydrodynamics. *Rev. Sci. Instrum.* **67** (1), 302–306.

DIMONTE, G. & RAMAPRABHU, P. 2010 Simulations and model of the nonlinear Richtmyer–Meshkov instability. *Phys. Fluids* **22** (1), 014104.

DIMONTE, G., TERRONES, G., CHERNE, F. J., GERMANN, T. C., DUPONT, V., KADAU, K., BUTTLER, W. T., ORO, D. M., MORRIS, C. & PRESTON, D. L. 2011 Use of the Richtmyer–Meshkov instability to infer yield stress at high-energy densities. *Phys. Rev. Lett.* **107** (25), 264502.

DRAKE, R. P. 2009 Perspectives of high energy density physics. *Phys. Plasmas* **16** (5), 055501.

EMMONS, H. W., CHANG, C. T. & WATSON, B. C. 1960 Taylor instability of finite surface waves. *J. Fluid Mech.* **7** (2), 177–193.

FRALEY, G. 1986 Rayleigh–Taylor stability for a normal shock-wave density discontinuity interaction. *Phys. Fluids* **29** (2), 376–386.

GLENDINNING, S. G., BOLSTAD, J., BRAUN, D. G., EDWARDS, M. J., HSING, W. W., LASINSKI, B. F., LOUIS, H., MILES, A., MORENO, J., PEYSER, T. A., REMINGTON, B. A., ROBEY, H. F., TURANO, E. J., VERDON, C. P. & ZHOU, Y. 2003 Effect of shock proximity on Richtmyer–Meshkov growth. *Phys. Plasmas* **10** (5), 1931–1936.

GONCHAROV, V. N. 2002 Analytical model of nonlinear, single-mode, classical Rayleigh–Taylor instability. *Phys. Rev. Lett.* **88** (13), 134502.

GRIFFOND, J. 2006 Linear interaction analysis for Richtmyer–Meshkov instability at low Atwood numbers. *Phys. Fluids* **18** (5), 054106.

GROVE, J. W., HOLMES, R., SHARP, D. H., YANG, Y. & ZHANG, Q. 1993 Quantitative theory of Richtmyer–Meshkov instability. *Phys. Rev. Lett.* **71** (21), 3473–3476.

HAAN, S. W. 1991 Weakly nonlinear hydrodynamic instabilities in inertial fusion. *Phys. Fluids* B **3** (8), 2349–2355.

HAZAK, G. 1996 Lagrangian formalism for the Rayleigh–Taylor instability. *Phys. Rev. Lett.* **76** (22), 4167–4170.

HECHT, J., ALON, U. & SHVARTS, D. 1994 Potential flow models of Rayleigh–Taylor and Richtmyer–Meshkov bubble fronts. *Phys. Fluids* **6** (12), 4019–4030.

HERRMANN, M. 2008 A balanced force refined level set grid method for two-phase flows on unstructured flow solver grids. *J. Comput. Phys.* **227** (4), 2674–2706.

HERRMANN, M. 2010 A parallel Eulerian interface tracking/Lagrangian point particle multi-scale coupling procedure. *J. Comput. Phys.* **229** (3), 745–759.

HERRMANN, M., MOIN, P. & ABARZHI, S. I. 2008 Nonlinear evolution of the Richtmyer–Meshkov instability. *J. Fluid Mech.* **612**, 311–338.

HOLMES, R. L., DIMONTE, G., FRYXELL, B., GITTINGS, M. L., GROVE, J. W., SCHNEIDER, M., SHARP, D. H., VELIKOVICH, A. L., WEAVER, R. P. & ZHANG, Q. 1999 Richtmyer–Meshkov instability growth: experiment, simulation and theory. *J. Fluid Mech.* **389**, 55–79.

HOLYER, J. Y. 1979 Large amplitude progressive interfacial waves. *J. Fluid Mech.* **93**, 433–448.

INGRAHAM, R. L. 1954 Taylor instability of the interface between superposed fluids – solution by successive approximations. *Proc. Phys. Soc.* B **67** (10), 748–752.

JACOBS, J. W. & CATTON, I. 1988 Three-dimensional Rayleigh–Taylor instability. 1. Weakly nonlinear theory. *J. Fluid Mech.* **187**, 329–352.

JACOBS, J. W., JENKINS, D. G., KLEIN, D. L. & BENJAMIN, R. F. 1995 Nonlinear growth of the shock accelerated instability of a thin fluid layer. *J. Fluid Mech.* **295**, 23–32.

JACOBS, J. W. & SHEELEY, M. 1996 Experimental study of incompressible Richtmyer–Meshkov instability. *Phys. Fluids* **8** (2), 405–415.

JIANG, G.-S. & PENG, D. 2000 Weighted ENO schemes for Hamilton–Jacobi equations. *SIAM J. Sci. Comput.* **21** (6), 2126–2143.

KADAU, K., BARBER, J. L., GERMANN, T. C., HOLIAN, B. L. & ALDER, B. J. 2010 Atomistic methods in fluid simulation. *Phil. Trans. R. Soc. Lond.* A **368**, 1547–1560.

KIVITY, Y. & HANIN, M. 1981 Stability of interface and shock-wave driven by initial pressure discontinuity. *Phys. Fluids* **24** (6), 1010–1016.

KOTELNIKOV, A. D., RAY, J. & ZABUSKY, N. J. 2000 Vortex morphologies on reaccelerated interfaces: visualization, quantification and modeling of one- and two-mode compressible and incompressible environments. *Phys. Fluids* **12** (12), 3245–3264.

LAYZER, D. 1955 On the instability of superposed fluids in a gravitational field. *Astrophys. J.* **122** (1), 1–12.

LIKHACHEV, O. A. & JACOBS, J. W. 2005 A vortex model for Richtmyer–Meshkov instability accounting for finite Atwood number. *Phys. Fluids* **17** (3), 031704.

MATSUOKA, C. 2010 Renormalization group approach to interfacial motion in incompressible Richtmyer–Meshkov instability. *Phys. Rev.* E **82** (3), 036320.

MATSUOKA, C. & NISHIHARA, K. 2006 Vortex core dynamics and singularity formations in incompressible Richtmyer–Meshkov instability. *Phys. Rev.* E **73** (2), 026304.

MATSUOKA, C., NISHIHARA, K. & FUKUDA, Y. 2003 Nonlinear evolution of an interface in the Richtmyer–Meshkov instability. *Phys. Rev.* E **67** (3), 036301; erratum, *Phys. Rev.* E, **68**(2) 029902.

MENIKOFF, R. & ZEMACH, C. 1983 Rayleigh–Taylor instability and use of conformal maps for ideal fluid flow. *J. Comput. Phys.* **51** (1), 28–64.

MESHKOV, E. E. 1969 Instability of the interface of two gases accelerated by a shock. *Fluid Dyn.* **4** (5), 101–104.

MESHKOV, E. E. 2006 *Studies of Hydrodynamic Instabilities in Laboratory Experiments* (in Russian), Sarov, FGYC-VNIIEF, ISBN 5-9515-0069-9.

MESHKOV, E. 2013 Some peculiar features of hydrodynamic instability development. *Phil. Trans. R. Soc. Lond.* A **371**, 20120288.

MEYER, K. A. & BLEWETT, P. J. 1972 Numerical investigation of the stability of a shock accelerated interface between two fluids. *Phys. Fluids* **15** (5), 753–759.

MIKAELIAN, K. O. 1994 Comment on quantitative theory of Richtmyer–Meshkov instability. *Phys. Rev. Lett.* **73** (23), 3177.

MIKAELIAN, K. O. 1998 Analytic approach to nonlinear Rayleigh–Taylor and Richtmyer–Meshkov instabilities. *Phys. Rev. Lett.* **80** (3), 508–511.

MIKAELIAN, K. O. 2003 Explicit expressions for the evolution of single-mode Rayleigh–Taylor and Richtmyer–Meshkov instabilities at arbitrary Atwood numbers. *Phys. Rev.* E **67** (2), 026319.

MIKAELIAN, K. O. 2008 Limitations and failures of the Layzer model for hydrodynamic instabilities. *Phys. Rev.* E **78** (1), 015303.

MUESCHKE, N., KRAFT, W. N., DIBUA, O., ANDREWS, M. J. & JACOBS, J. W. 2005 Numerical investigation of single-mode Richtmyer–Meshkov instability. In *Proceedings of the ASME Fluids Engineering Division Summer Conference—2005*, vol. 1, Pts A and B, pp. 185–193.

NEUVAZHAEV, V. YE. & PARSHUKOV, I. E. 1992 Study of the Richtmyer–Meshkov instability by the vortex method. In *Mathematical Modelling and Applied Mathematics, Proceedings of the IMACS International Conference on Mathematical Modelling and Applied Mathematics, Moscow, USSR, 18–23 June 1990* (ed. A. A. Samarsky & M. P. Sapagovas), pp. 323–335. North-Holland.

NIEDERHAUS, C. E. & JACOBS, J. W. 2003 Experimental study of the Richtmyer–Meshkov instability of incompressible fluids. *J. Fluid Mech.* **485**, 243–277.

NISHIHARA, K., WOUCHUK, J. G., MATSUOKA, C., ISHIZAKI, R. & ZHAKHOVSKY, V. V. 2010 Richmyer–Meshkov instability: theory of linear and nonlinear evolution. *Phil. Trans. R. Soc. Lond.* A **368** (1916), 1769–1807.

OLSON, D. H. & JACOBS, J. W. 2009 Experimental study of Rayleigh–Taylor instability with a complex initial perturbation. *Phys. Fluids* **21** (3), 034103.

ORON, D., ARAZI, L., KARTOON, D., RIKANATI, A., ALON, U. & SHVARTS, D. 2001 Dimensionality dependence of the Rayleigh–Taylor and Richtmyer–Meshkov instability late-time scaling laws. *Phys. Plasmas* **8** (6), 2883–2889.

PELZ, R. B. & GULAK, Y. 1997 Evidence for a real-time singularity in hydrodynamics from time series analysis. *Phys. Rev. Lett.* **79** (24), 4998–5001.

PENG, D., MERRIMAN, B., OSHER, S., ZHAO, H. & KANG, M. 1999 A PDE-based fast local level set method. *J. Comput. Phys.* **155** (2), 410–438.

REMINGTON, B. A., DRAKE, R. P. & RYUTOV, D. D. 2006 Experimental astrophysics with high power lasers and Z-pinches. *Rev. Mod. Phys.* **78** (3), 755–807.

RICHTMYER, R. D. 1960 Taylor instability in shock acceleration of compressible fluids. *Commun. Pure Appl. Maths* **13** (2), 297–319.

RIKANATI, A., ORON, D., SADOT, O. & SHVARTS, D. 2003 High initial amplitude and high Mach number effects on the evolution of the single-mode Richtmyer–Meshkov instability. *Phys. Rev.* E **67** (2), 026307.

ROSENHEAD, L. 1931 The formation of vortices from a surface of discontinuity. *Proc. R. Soc. Lond.* A **134** (823), 170–192.

SADOT, O., EREZ, L., ALON, U., ORON, D., LEVIN, L. A., EREZ, G., BEN-DOR, G. & SHVARTS, D. 1998 Study of nonlinear evolution of single-mode and two bubble interaction under Richtmyer–Meshkov instability. *Phys. Rev. Lett.* **80** (8), 1654–1657.

SCHWARTZ, L. W. 1974 Computer extension and analytic continuation of Stokes' expansion for gravity waves. *J. Fluid Mech.* **62**, 553–578.

SHU, C. W. 1988 Total-variation-diminishing time discretization. *SIAM J. Sci. Stat. Comput.* **9** (6), 1073–1084.

SOHN, S.-I. 2003 Simple potential-flow model of Rayleigh–Taylor and Richtmyer–Meshkov instabilities for all density ratios. *Phys. Rev.* E **67** (2), 026301.

SOHN, S.-I. 2004 Density dependence of a Zufiria-type model for Rayleigh–Taylor bubble fronts. *Phys. Rev.* E **70** (4), 045301.

SOHN, S.-I. 2008 Density dependence of a Zufiria-type model for Rayleigh–Taylor bubble fronts. *Phys. Rev.* E **78** (1), 017302.

SOHN, S.-I. 2009 Effects of surface tension and viscosity on the growth rates of Rayleigh–Taylor and Richtmyer–Meshkov instabilities. *Phys. Rev.* E **80** (5), 055302.

SREENIVASAN, K. R. 1999 Fluid turbulence. *Rev. Mod. Phys.* **71** (2), S383–S395.

STANIC, M., MCFARLAND, J., STELLINGWERF, R. F., CASSIBRY, J. T., RANJAN, D., BONAZZA, R., GREENOUGH, J. A. & ABARZHI, S. I. 2013 Non-uniform volumetric structures in Richtmyer–Meshkov flows. *Phys. Fluids* **25**, 106107.

STANIC, M., STELLINGVERF, R. F., CASSIBRY, J. T. & ABARZHI, S. I. 2012 Scale coupling in Richtmyer–Meshkov flows induced by strong shocks. *Phys. Plasmas* **19** (8), 082706.

STOKES, G. G. 1849 On the theory of oscillatory waves. *Trans. Camb. Phil. Soc.* **8**, 441–455.

SUSSMAN, M., SMEREKA, P. & OSHER, S. 1994 A level set method for computing solutions to incompressible two-phase flow. *J. Comput. Phys.* **114** (1), 146–159.

VANDENBOOMGAERDE, M., GAUTHIER, S. & MÜGLER, C. 2002 Nonlinear regime of a multimode Richtmyer–Meshkov instability: a simplified perturbation theory. *Phys. Fluids* **14** (3), 1111–1122.

VANDENBOOMGAERDE, M., MÜGLER, C. & GAUTHIER, S. 1998 Impulsive model for the Richtmyer–Meshkov instability. *Phys. Rev.* E **58** (2), 1874–1882.

VAN DER PIJL, S. P., SEGAL, A., VUIK, C. & WESSELING, P. 2005 A mass-conserving Level–Set method for modelling of multi-phase flows. *Intl J. Numer. Meth. Fluids* **47** (4), 339–361.

VELIKOVICH, A. L. 1996 Analytic theory of Richtmyer–Meshkov instability for the case of reflected rarefaction wave. *Phys. Fluids* **8** (6), 1666–1679.

VELIKOVICH, A. L. & DIMONTE, G. 1996 Nonlinear perturbation theory of the incompressible Richtmyer–Meshkov instability. *Phys. Rev. Lett.* **76** (17), 3112–3115.

VELIKOVICH, A. & PHILLIPS, L. 1996 Instability of a plane centered rarefaction wave. *Phys. Fluids* **8** (4), 1107–1118.

VOLKOV, N. B., MAĬER, A. E. & YALOVETS, A. P. 2001 The nonlinear dynamics of the interface between media possessing different densities and symmetries. *Tech. Phys. Lett.* **27** (1), 20–24.

VOLKOV, N. B., MAĬER, A. E. & YALOVETS, A. P. 2003 Nonlinear dynamics of the interface between continuous media with different densities. *Tech. Phys. Lett.* **48** (3), 275–283.

WHITE, J., OAKLEY, J., ANDERSON, M. & BONAZZA, R. 2010 Experimental measurements of the nonlinear Rayleigh–Taylor instability using a magnetorheological fluid. *Phys. Rev.* E **81** (2), 026303.

WOUCHUK, J. G. 2001*a* Growth rate of the linear Richtmyer–Meshkov instability when a shock is reflected. *Phys. Rev.* E **63** (5), 056303.

WOUCHUK, J. G. 2001*b* Growth rate of the Richtmyer–Meshkov instability when a rarefaction is reflected. *Phys. Plasmas* **8** (6), 2890–2907.

WOUCHUK, J. G. & CARRETERO, R. 2004 Linear perturbation growth at the trailing edge of a rarefaction wave. *Phys. Plasmas* **10** (11), 4237–4252.

WU, S. J. 1999 Well-posedness in Sobolev spaces of the full water wave problem in 3-D. *J. Am. Math. Soc.* **12** (2), 445–495.

YANG, Y., ZHANG, Q. & SHARP, D. 1994 Small amplitude theory of Richtmyer–Meshkov instability. *Phys. Fluids* **6** (5), 1856–1873.

ZABUSKY, N. J., KOTELNIKOV, A. D., GULAK, Y. & PENG, G. 2003 Amplitude growth rate of Richtmyer–Meshkov unstable two-dimensional interface to intermediate times. *J. Fluid Mech.* **475**, 147–162.

ZHANG, Q. 1998 Analytical solutions of Layzer-type approach to unstable interfacial fluid mixing. *Phys. Rev. Lett.* **81** (16), 3391–3394.

ZHANG, Q. & SOHN, S.-I. 1996 An analytical nonlinear theory of Richtmyer–Meshkov instability. *Phys. Lett.* A **212** (3), 149–155.

ZHANG, Q. & SOHN, S.-I. 1997*a* Nonlinear theory of unstable fluid mixing driven by shock wave. *Phys. Fluids* **9** (4), 1106–1124.

ZHANG, Q. & SOHN, S.-I. 1997*b* Padé approximation to an interfacial fluid mixing problem. *Appl. Math. Lett.* **10** (5), 121–127.

ZHANG, Q. & SOHN, S.-I. 1999 Quantitative theory of Richtmyer–Meshkov instability in three dimensions. *Z. Angew. Math. Phys.* **50**, 1–46.

ZUFIRIA, J. A. 1988 Bubble competition in Rayleigh–Taylor instability. *Phys. Fluids* **31** (3), 440–446.